

EVOLUTION OF CIV ABSORBERS. I. THE COSMIC INCIDENCE

FARHANUL HASAN,¹ CHRISTOPHER W. CHURCHILL,¹ BRYSON STEMOCK,¹ NIGEL L. MATHES,¹ NIKOLE M. NIELSEN,^{2,3}
KRISTIAN FINLATOR,¹ MARK CROOM,¹ GLENN G. KACPRZAK,^{2,3} AND MICHAEL T. MURPHY²

¹*Department of Astronomy, New Mexico State University, Las Cruces, NM 88003, USA*

²*Centre for Astrophysics and Supercomputing, Swinburne University of Technology, Hawthorn, Victoria 3122, Australia*

³*ARC Centre of Excellence for All Sky Astrophysics in 3 Dimensions (ASTRO 3D)*

(Received July 22, 2020)

Submitted to ApJ

ABSTRACT

We present a large high-resolution study of the distribution and evolution of CIV absorbers, including the weakest population with equivalent widths $W_r < 0.3 \text{ \AA}$. By searching 369 high-resolution, high signal-to-noise spectra of quasars at $1.1 \leq z_{\text{em}} \leq 5.3$ from Keck/HIRES and VLT/UVES, we find 1318 CIV absorbers with $W_r \geq 0.05 \text{ \AA}$ (our $\sim 50\%$ completeness limit) at redshifts $1.0 \leq z \leq 4.75$. A Schechter function describes the observed equivalent width distribution with a transition from power-law to exponential decline at $W_r \gtrsim 0.5 \text{ \AA}$. The power-law slope α rises and normalization n_* falls by $\sim 20\%$ from $1.0 \leq z < 2.5$ to $2.5 \leq z \leq 4.75$. We find that the co-moving redshift path density, dN/dX , of $W_r \geq 0.05 \text{ \AA}$ absorbers rises by ~ 1.8 times from $z = 4.75$ to $z = 1$, while the increase in the $W_r \geq 0.6 \text{ \AA}$ dN/dX is ~ 4.5 times as much. We quantify the observed evolution by a model in which dN/dX decreases linearly with increasing redshift. The model suggests that populations with larger W_r thresholds evolve faster with redshift and appear later in the universe. The cosmological TECHNICOLOR DAWN simulations at $3 \leq z \leq 5$ over-produce the observed abundance of absorbers with $W_r \leq 0.3 \text{ \AA}$, while yielding good agreement at higher W_r . Our empirical linear model successfully describes CIV evolution in the simulations and the observed evolution of $W_r \geq 0.6 \text{ \AA}$ CIV for the past ~ 12 Gyr. Combining our measurements with the literature gives us a picture of CIV-absorbing structures becoming more numerous and/or larger in physical size over the last ≈ 13 Gyr of cosmic time ($z \sim 6$ to $z \sim 0$).

Keywords: galaxies: halos — galaxies: evolution — galaxies: intergalactic medium — quasars: absorption lines – techniques: spectroscopic

1. INTRODUCTION

The processing of baryons within and between galaxies is fundamental to how galaxies form and evolve, and is an important phenomenon in shaping the universe as we observe it today. Obtaining a detailed census of the cosmic distribution and evolution of metal-enriched gas is a key step in understanding this “baryon cycle”.

According to our current understanding, metals form in stars within galaxies and are expelled out to the circumgalactic medium (CGM) and the intergalactic medium (IGM) via a variety of feedback processes (e.g., Lilly et al. 2013; Dekel & Mandelker 2014; Somerville & Davé 2015; Finlator 2017). Over billions of years, some of these metals are recycled back into the galaxies whence they originated, possibly repeating the cycle

several times, whereas others may escape the galaxy and enter the IGM (e.g., Oppenheimer & Davé 2008; Ford et al. 2014; Muratov et al. 2015, 2017). Some fraction of these metals in the IGM may eventually accrete into the CGM or interstellar medium of other galaxies (e.g., Oppenheimer et al. 2010; Brook et al. 2014; Anglés-Alcázar et al. 2017). Metals in the gas phase are therefore an invaluable and crucial tracer of the baryon cycle (e.g., Steidel 1993; Churchill et al. 1999; Kacprzak et al. 2012; Nielsen et al. 2015; Christensen et al. 2016; Tumlinson et al. 2017; Lehner et al. 2019).

Fortunately, CGM and IGM gas-phase metals are directly observable using quasar absorption-line spectroscopy, as long as the gas is intervening to the line of sight of a background quasar. The CIV $\lambda\lambda 1548, 1550$ resonant fine-structure doublet is one of the most commonly observed metal absorption features in quasar spectra, and has been studied extensively over the red-

Corresponding author: Farhanul Hasan
farhasan@nmsu.edu

shift range $0 \lesssim z \lesssim 6.5$ (e.g., Sargent et al. 1988; Steidel 1990; Petitjean & Bergeron 1994; Rauch et al. 1996; Chen et al. 2001; Schaye et al. 2003; Adelberger et al. 2005; Songaila 2005; Scannapieco et al. 2006; Becker et al. 2009; Cooksey et al. 2010, 2013; D’Odorico et al. 2010, 2013; Bordoloi et al. 2014; Burchett et al. 2015; Boksenberg & Sargent 2015; Codoreanu et al. 2018; Cooper et al. 2019).

The measured global cosmic evolution of CIV absorbers provides insights into the universal carbon content of the universe (e.g., Danforth & Shull 2008; Simcoe 2011; Rafelski et al. 2012) and the ionizing ultraviolet background (UVB, e.g., Faucher-Giguère et al. 2009; Haardt & Madau 2012; Becker & Bolton 2013; Doughty et al. 2018) as traced by moderately low density warm temperature gas structures, i.e., $\log n_{\text{H}} \sim -3$ [cm^{-3}] and $\log T \sim 4.8$ [K] (e.g., Steidel 1990; Bergeron & Herbert-Fort 2005; Churchill et al. 2015). Two of the most important quantities that quantify the distribution and evolution of CIV absorbing gas are the co-moving path number density, dN/dX , which is the number of absorbers per unit “absorption path” (Bahcall & Peebles 1969), and the equivalent width distribution (EWD), which provides the number of absorbers per unit equivalent width per unit absorption path ($d^2N/dWdX$).

To date, the largest survey of CIV absorbers was conducted by Cooksey et al. (2013, hereafter C13), who located $\sim 15,000$ absorbers at $1.5 \lesssim z \lesssim 4.5$ in $\sim 26,000$ quasar spectra from the Sloan Digital Sky Survey (SDSS, York et al. 2000), comprising a co-moving path length $\Delta X \simeq 38,600$. They placed robust constraints on the evolution of strong absorbers, i.e., those with rest-frame CIV $\lambda 1548$ equivalent widths $W_r(\lambda 1548) \geq 0.6$ Å (hereafter, W_r). Their sensitivity to detecting smaller W_r absorbers decreased quickly for $W_r < 0.6$ Å, reaching $\sim 20\%$ completeness at $W_r = 0.3$ Å.

For $W_r \geq 0.6$ Å absorbers, C13 found that dN/dX increased by a factor of ≈ 2.5 from $z = 4.5$ to $z = 1$. Their highly constrained measurement of the increase in dN/dX with cosmic time is consistent with the trends of less constraining findings from smaller surveys (e.g., Sargent et al. 1988; Misawa et al. 2002; Péroux et al. 2004; D’Odorico et al. 2016), some of which probed smaller W_r thresholds. Incorporating absorbers with $W_r \geq 0.3$ Å, C13 found that the EWD is well-described by an exponential function, a result consistent with the earliest surveys (Sargent et al. 1988; Steidel 1990).

Unfortunately, the available information characterizing “weak” CIV absorbers with $W_r < 0.3$ Å across various redshift ranges is limited (Schaye et al. 2003, 2007; Scannapieco et al. 2006; Cooksey et al. 2010; D’Odorico et al. 2010; Boksenberg & Sargent 2015; Burchett et al. 2015). As such, the distribution, statistical properties, and evolution of the $W_r < 0.3$ Å regime of CIV is yet to be fully characterized. Charting this regime is important, as it probes moderately low density warm gas structures optically thin to hydrogen and helium ioniz-

ing photons from the ionizing spectrum, which means sensitivity to the evolving shape of the UVB can be directly probed with cosmic time. Furthermore, dN/dX of weak CIV absorbers can, in a statistical sense, inform us of the distribution of carbon and other metals in optically thin gas structures relative to galaxies as a function of redshift.

Hydrodynamic cosmological simulations have often used CIV as a target metal-line absorber to test theoretical predictions against observations, hence improving our understanding of the baryon cycle in the broader context of galaxy evolution (e.g., Oppenheimer & Davé 2008; Oppenheimer et al. 2009; Cen & Chisari 2011; Finlator et al. 2015, 2020). One of the reasons for this is the high cosmic abundance and oscillator strength of the C^{+3} ion. Moreover, C^{+3} serves as a higher-energy complement to the Ly α forest as a probe of the metagalactic UVB, due to the ground-state ionization potential of C^{+2} and C^{+3} being 3.5 Ryd and 4.7 Ryd, respectively. CIV is also an independent probe in the ionization energy range of He^0 (1.8 Ryd) and He^+ (4.0 Ryd). Providing as stringent observational constraints as possible on the distribution, incidence, and evolution of the broad range of CIV absorbing gas structures will be key to driving such studies and progressing our understanding of the distribution of metals and the evolution of the ionizing UVB.

To improve the global statistics of CIV absorbers and provide robust statistics of weak absorbers, we searched for CIV $\lambda\lambda 1548, 1550$ doublet absorption in several hundred high-resolution quasar spectra from both the Keck/HIRES (Vogt et al. 1994) and VLT/UVES (Dekker et al. 2000) instruments. We employed an automated line detection approach similar to that of Zhu & Ménard (2013) and intensive visual inspection to identify and verify each absorption doublet. The high sensitivity of our survey allows us to probe the distribution and evolution of CIV absorbers an order of magnitude weaker than those studied by C13 (whose spectral resolution was $\gtrsim 20$ times lower). In summary, we analyzed over 1300 CIV absorbers with $W_r \geq 0.05$ Å spanning redshifts $1.0 \leq z \leq 4.75$ identified in the HIRES and UVES spectra of 369 quasars distributed over redshifts $1.1 \leq z_{\text{em}} \leq 5.3$.

In this paper, we present our survey methods and results, and our inferences about the nature of CIV absorbers. The survey design, methods for identifying CIV absorption doublets, calculation of the redshift-dependent sensitivity and detection completeness limits, and measurements of the absorption properties are presented in Section 2. In Section 3, we describe our analysis methods and present the observed EWD and dN/dX of CIV absorbers. We also introduce an empirical model to quantify the observed evolution. In Section 4, we discuss the observed evolution and our model extrapolations, draw from the literature to augment the redshift range of our survey, and compare our observations with

a mock CIV survey generated from the TECHNICALOR DAWN hydrodynamic cosmological simulations (Finlator et al. 2018). We provide our concluding remarks in Section 5. When necessary, and for consistent comparison with C13, we adopt the WMAP5 cosmology, with $H_0 = 71.9 \text{ km s}^{-1} \text{ Mpc}^{-1}$, $\Omega_M = 0.258$, and $\Omega_\Lambda = 0.742$ (Komatsu et al. 2009).

2. DATA AND ANALYSIS

2.1. Quasar spectra

We have analyzed 369 high resolution, high signal-to-noise quasar spectra obtained with the HIRES spectrograph (Vogt et al. 1994) and the UVES spectrograph (Dekker et al. 2000) from the Keck and Very Large Telescope (VLT) observatories, respectively. The wavelength coverage of the spectra spans approximately 3000 – 10000 Å, though there is variable coverage in this range from spectrum to spectrum. The resolving power of both HIRES and UVES is $R = \lambda/\Delta\lambda \approx 45000$, or $\sim 6.6 \text{ km s}^{-1}$, with 3 pixels per FWHM resolution element. The FWHM velocity resolution is approximately constant as a function of observed wavelength. The signal-to-noise ratios are typically 25 – 80 per pixel.

Roughly half of the Keck/HIRES spectra were obtained from various observing programs prior to the creation of the Keck Observatory Archive,¹ some having been donated in science-ready form by Charles Steidel, J. Xavier Prochaska, Christopher Churchill, Michael Rauch and the late Wallace Sargent. The remaining Keck/HIRES spectra were obtained from Data Release 1 of the KODIAQ project (O’Meara et al. 2015). The VLT/UVES spectra were acquired through the efforts of the UVES SQUAD prior to their Data Release 1 (Murphy et al. 2019).

The journal of quasar spectra used in this study is listed in Table 1. For each quasar, the columns list (1) the quasar name, taken from Véron-Cetty & Véron (2001), (2) the emission redshift, (3) the instrument with which the spectrum was obtained, (4) the minimum wavelength of the CIV search space in the spectrum, set by Ly α $\lambda 1215$ emission of the quasar (see Section 2.3), and (5) the maximum wavelength of the CIV search space, set by 3000 km s^{-1} blueward of the CIV $\lambda 1548$ emission of the quasar (Section 2.3).

2.2. Reduction of Spectra

The KODIAQ spectra were reduced according to the prescriptions of O’Meara et al. (2015). The spectra of Churchill were reduced using the standard Image Reduction and Analysis Facility (IRAF²), as outlined in Churchill (1997). Those of Sargent, Rauch, Prochaska, and Steidel were reduced using the Mauna Kea Echelle

¹ <https://www2.keck.hawaii.edu/koa/public/koa.php>

² IRAF is distributed by the National Optical Astronomy Observatories, which are operated by the Association of Universities for Research in Astronomy, Inc., under cooperative agreement with the National Science Foundation.

Table 1. Journal of Observations

Quasar	z_{em}	Instrument(s)	λ_{min}^a (Å)	λ_{max}^b (Å)
J002830–281704	2.400	HIRES	4133	5211
J064632+445116	3.408	UVES	5358	6756
J010104–285801	3.070	UVES	4947	6238
J102325+514251	3.447	HIRES	5406	6815
J105744+062914	3.142	UVES	5035	6348
J110045+112239	4.707	HIRES	6937	8747
J120207+323538	5.292	HIRES	7648	9643
J155556+480015	3.299	HIRES	5226	6589
J201717–401924	4.131	UVES	6237	7864
J235714–273659	1.732	UVES	3321	4187

^a Minimum wavelength of CIV search space, defined by Ly α $\lambda 1215$ emission of the quasar (see Section 2.3) ^b Maximum wavelength of CIV search space, 3000 km s^{-1} blueward of the CIV $\lambda 1548$ emission of the quasar

NOTE—Table 1 is published in its entirety in machine-readable format. A portion containing a representative selection of quasars is shown here for guidance regarding its form and content.

Extraction (MAKEE) data reduction package, developed by Tom Barlow (Barlow 2005), which is optimized for the spectral extraction of single, unresolved point sources. All HIRES spectra were wavelength calibrated using ThAr lamps to the vacuum heliocentric standard at rest and were continuum fit by their respective donors.

The UVES spectra were reduced using the UVES pipeline in the MIDAS environment (Dekker et al. 2000), which is provided by the European Southern Observatory (ESO). The wavelength solution is determined using a standard ThAr lamp exposure corrected to vacuum heliocentric velocities. The individual exposures were then combined into one-dimensional spectra using the UVES PPost-Pipeline Echelle Reduction (UVES_POPLER) software (Murphy 2016; Murphy et al. 2019).

Using the interactive mode of the POPLER software, we examined and refined the continuum fits for all quasar spectra with particular attention to the spectral regions redward of the quasar Ly α $\lambda 1215$ emission line following the prescriptions of King et al. (2012) and Murphy et al. (2016). An example UVES spectrum of the $z_{em} = 3.130$ quasar J103909–231326 is shown in Figure 1. Strong emission lines are labelled, and the spectral region where we searched for CIV $\lambda\lambda 1548, 1550$ doublet lines is shown (see Section 2.3). CIV absorbers detected at different redshifts are highlighted.

2.3. Identifying and Verifying Absorption Doublets

We surveyed the spectra for the CIV $\lambda\lambda 1548, 1550$ resonance doublet. Such high quality spectra allow for an in-depth investigation into the cosmic frequency of the very weakest CIV absorbers, a regime that heretofore

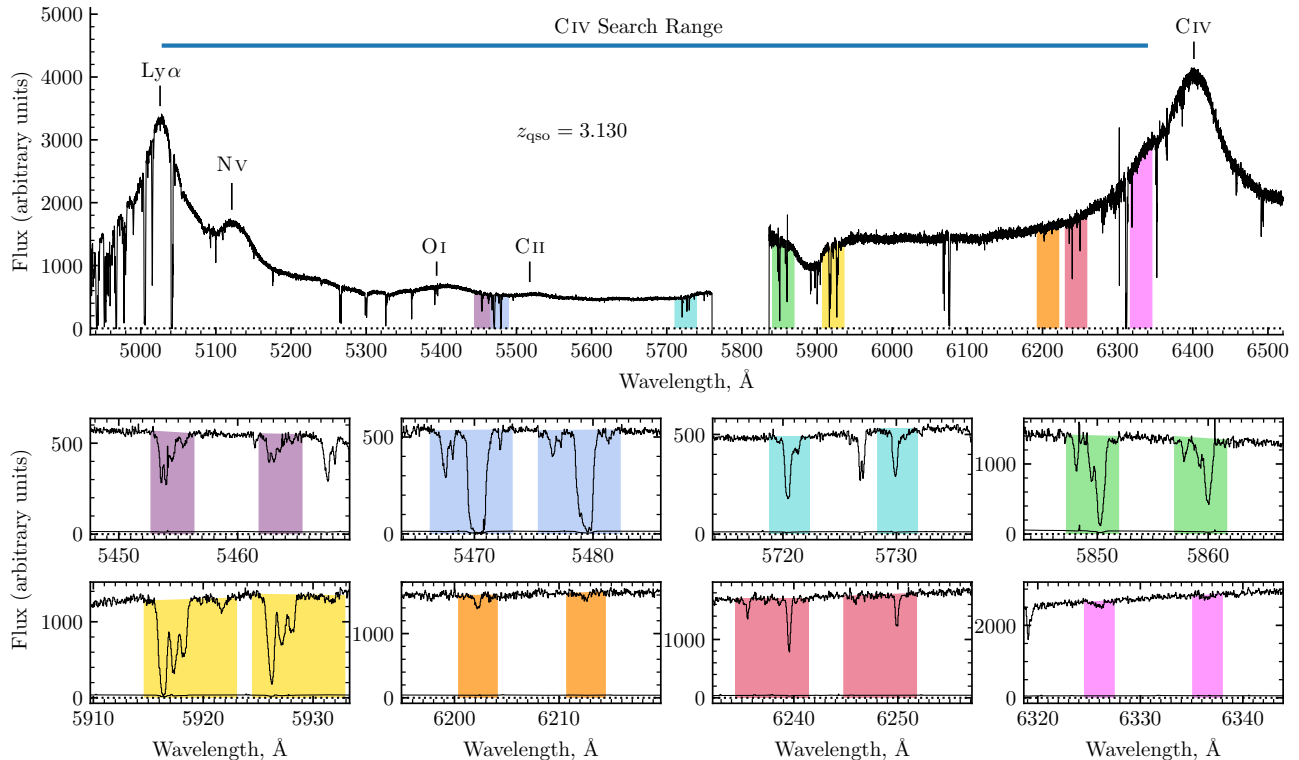


Figure 1. An example spectrum of the quasar J103909–231326 at $z_{\text{em}} = 3.130$ observed with VLT/UVES and eight of its C IV $\lambda\lambda 1548, 1550$ doublets presented in redshift order, $z = 2.5228$ (purple), $z = 2.5333$ (blue), $z = 2.6949$ (teal), $z = 2.7787$ (green), $z = 2.8216$ (yellow), $z = 3.0061$ (orange), $z = 3.0302$ (red), and $z = 3.0861$ (magenta). The search range for C IV doublets is indicated, as are some emission lines from the quasar. Note the coverage gap at $\sim 5760\text{--}5840$ Å.

has not been explored in great detail.

To detect intervening C IV $\lambda\lambda 1548, 1550$ absorption in our quasar spectra, we confined the search range to regions of the spectrum redward of the Ly α emission, as Ly α forest contamination would render automated detection of weak metal lines nearly impossible. To avoid selecting C IV absorbers associated with the quasar environment, we also restrict our absorbers to those blueshifted by $\Delta v_{\text{QSO}} > 3000$ km s $^{-1}$ from the quasar emission redshift. Finally, strong telluric absorption bands at 6868–6932 Å (B-band) and 7594–7700 Å (A-band) are excluded as these molecular lines can have separations and ratios leading to false positives when searching for C IV doublets.

Our automated search routine is based on the methods of Zhu & Ménard (2013). We performed a matched filter search for C IV $\lambda\lambda 1548, 1550$ doublet candidates detected by signals exceeding 5σ in local noise of the resulting output signal spectrum. We used a two-component top hat filter separated by the wavelength difference of the C IV doublet, where each component has a width of seven pixels, which is 2.33 times the FWHM of an unresolved absorption feature. We convolved the filter with the normalized spectrum to generate the output signal spectrum in redshift space.

To measure the uncertainty in the output signal spec-

trum at a given pixel, we examined a $\Delta z \simeq 0.01$ region corresponding to roughly 3000 pixels centered on the pixel. We used iterative sigma-clipping (1σ) to remove outlier signals, leaving only the continuum of the output signal spectrum. We calculated the standard deviation of this continuum and adopted it as the noise in the output spectrum at the centered pixel. Further details are provided in Mathes (2017).

We also measured the equivalent width detection limit as a function of redshift for all quasar spectra. For each spectrum, we inserted Gaussian C IV absorption doublets in intervals of seven pixels. We assumed a Gaussian width, σ_l , equal to the instrumental line spread function to represent unresolved absorption lines. We then solved for the amplitude, A_l , of the Gaussian required to detect the unresolved line at a 5σ significance level with our matched filtering technique. Finally, we integrated to find the equivalent width, $W = \sqrt{2\pi} A_l \sigma_l$, which we adopted as the minimum detectable *observed* equivalent width at that redshift. Converting to the rest-frame equivalent width at each redshift yielded the detection threshold spectra. These spectra allow us to accurately characterize the completeness of our sample and are instrumental in quantifying the redshift path covered by the survey.

Once candidate C IV features are flagged, we define an

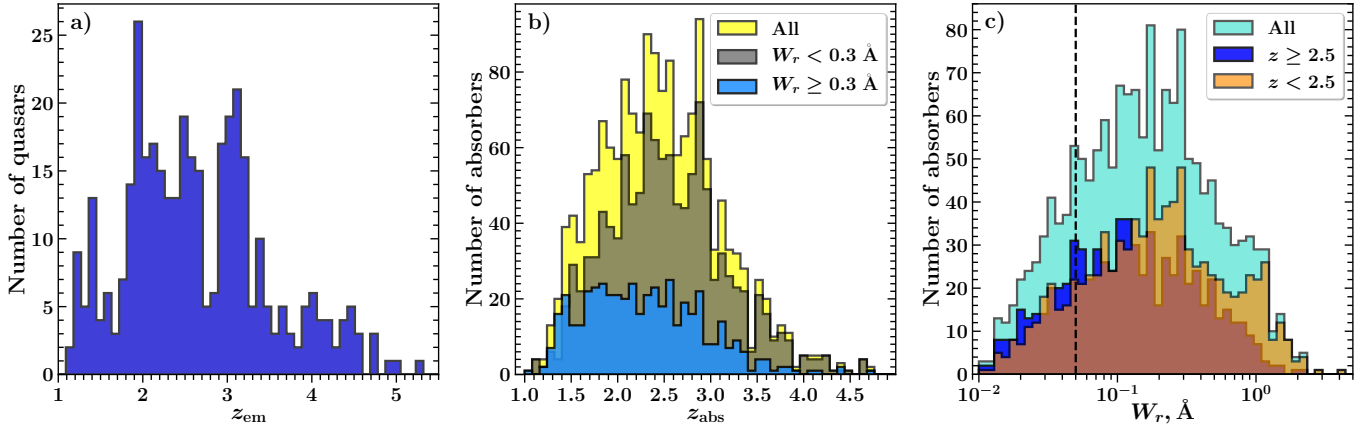


Figure 2. (a) The distribution of quasar emission redshifts, z_{em} . (b) The distribution of CIV absorber redshifts, z_{abs} . Weak absorbers, i.e., those with $W_r < 0.3 \text{ \AA}$ (shown in dark grey), are unique to this survey. (c) The distribution of rest-frame equivalent widths, W_r , for all redshifts ($1.0 \leq z < 4.75$), $z < 2.5$, and $z \geq 2.5$. The vertical dashed line is $W_r = 0.05 \text{ \AA}$, where the full survey is 50% complete (see Figure 4).

“absorber” to include all absorption in CIV $\lambda\lambda 1548, 1550$ lines detected within $\pm 500 \text{ km s}^{-1}$ of one another. As the rest-frame velocity separation of the CIV doublet is $\Delta v = 498 \text{ km s}^{-1}$, we did find a few self-blended absorbers.

Each candidate absorber was examined visually using our interactive graphical software SYSANAL (see Churchill 1997; Churchill et al. 1999; Churchill & Vogt 2001). In SYSANAL, the absorption profiles of the doublets are aligned in velocity space. Following the methods of Schneider et al. (1993), the software employs the “equivalent width spectrum” to objectively locate the absorption features. We used a 5σ significance level for the $\lambda 1548$ transition and a 3σ significance level for the $\lambda 1550$ transition, where the latter is examined only in the velocity range over which $\lambda 1548$ absorption is detected. Adopting the method described in Churchill et al. (1999) and Churchill & Vogt (2001), the velocity extremes of each absorption feature are determined when the equivalent width spectrum returns to the 1σ level. Following visual inspection and possible editing of the defined absorption regions, the software calculates the optical depth-weighted median absorption redshift, z_{abs} , setting the final velocity zero point for the absorption (see Churchill & Vogt 2001). Also computed are the equivalent widths of the doublet members, apparent optical depth (AOD) column density, and doublet ratios.

With the absorber redshift determined, we examined the full quasar spectrum using our software SEARCH (see Churchill et al. 1999) to examine whether associated absorption accompanied the CIV absorption. This helped us identify associated transitions such as Ly α $\lambda 1215$, SiIV $\lambda\lambda 1393, 1402$, MgII $\lambda\lambda 2796, 2803$, or other quasar absorption lines commonly found in metal-bearing gas clouds.

For an absorber to be included in our final science

Table 2. CIV Absorbers

Quasar	z_{abs}^a	W_r (\AA) ^b	$\log N^c$
J000149–015940	2.0107	0.082 ± 0.002	$13.44^{+0.09}_{-0.10}$
J003501–091817	2.2211	0.261 ± 0.009	$13.92^{+0.03}_{-0.04}$
J074927+415242	2.7650	0.153 ± 0.009	$13.68^{+0.02}_{-0.03}$
J111727–083857	4.0481	0.422 ± 0.018	$14.16^{+0.02}_{-0.04}$
J115411+063426	2.5634	0.058 ± 0.003	$13.24^{+0.06}_{-0.07}$
J123055–113909	3.2060	0.088 ± 0.007	$13.41^{+0.04}_{-0.06}$
J164656+551445	3.2887	0.167 ± 0.007	$13.68^{+0.02}_{-0.03}$
J214222–441929	2.8526	0.498 ± 0.013	$14.30^{+0.02}_{-0.03}$
J225719–100104	1.6613	0.259 ± 0.007	$14.07^{+0.03}_{-0.04}$
J235702–004824	2.7448	0.054 ± 0.006	$13.16^{+0.04}_{-0.07}$

^a Absorber redshift ^b Equivalent width of the CIV $\lambda 1548$ transition ^c AOD column density

NOTE—Table 2 is published in its entirety in machine-readable format. A portion containing a representative selection of absorbers is shown here for guidance regarding its form and content.

sample, we employed a three-person iterative inspection system. Each of the three individuals (F.H., B.S., and C.W.C.) was assigned a subset of candidate absorbers for which they were the primary inspector. The primary inspector would assign a rating of 0 to 10 for each of the candidate CIV absorbers, where 0 indicated zero confidence and 10 indicated total confidence in the reality of the CIV absorber. In particular, it was checked whether the doublet ratios, $W_r(1548)/W_r(1551)$, were between 1 and 2 (within uncertainties) as expected from the oscillator strengths of the doublet members. Alignment of the absorption profile shapes in velocity space was another critical aspect of this check. The primary inspector also provided a second rating of 0 to 10 in their confidence in

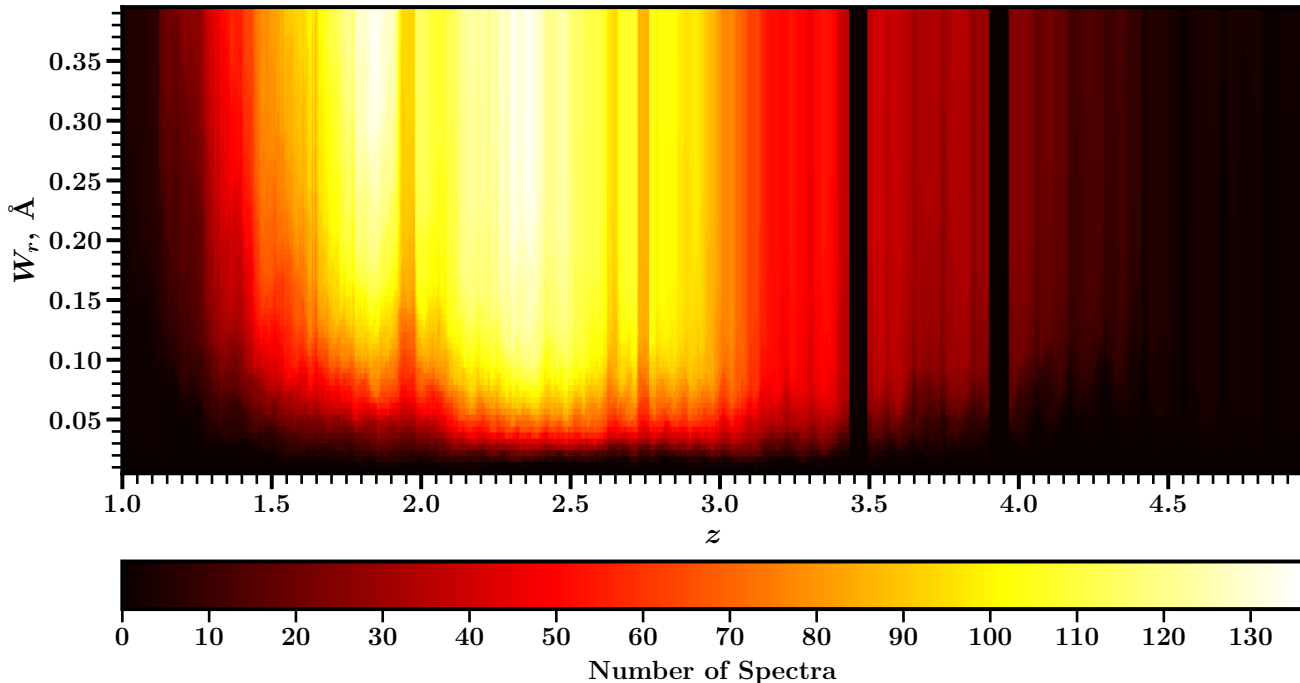


Figure 3. The sensitivity function, $g(W_r, z)$. The heat map details the number of quasar spectra in which we could have detected CIV absorption with a rest-frame equivalent width of W_r or greater at redshift z at the 3σ significance level. Note the dark vertical bands at $z \sim 3.5$ and $z \sim 3.9$ are due to the excluded atmospheric B and A bands, respectively.

the velocity limits obtained with SYSANAL as described above. These limits are critical in defining which pixels are included in the equivalent width calculations.

A rating of (10, 10) ensured inclusion into the science sample without further inspection, and a rating of (0, 0) ensured exclusion without further inspection. Any other ratings would require an independent assessment from a secondary inspector. The corroboration of associated transitions was taken as a strong indicator for a true CIV absorber. If consensus could not be achieved as to the reality of the absorber, then the third inspector would arbitrate while all three individuals inspected and discussed the absorber. Through this process, we located a total of 1625 CIV absorbers. For our final science sample, we use 1318 absorbers with equivalent widths above our 50% completeness level of $W_r = 0.05 \text{ \AA}$ (see Section 2.6).

In Table 2, we list the 1318 absorbers included in our final science sample. The columns are (1) the quasar name, (2) the absorption redshift, (3) the rest-frame equivalent width of the CIV $\lambda 1548$ transition, W_r , and (4) the AOD column density, $\log N$.

2.4. Sample Characteristics

In Figure 2(a), we show the distribution of quasar emission redshifts, z_{em} . In Figure 2(b), we present the distribution of absorber redshifts, z_{abs} , for our sample of CIV absorbers. As this survey is the first large survey sensitive to “weak” absorbers, i.e., those with $W_r < 0.3 \text{ \AA}$, we indicate the distribution of redshifts for

those absorbers below and above $W_r = 0.3 \text{ \AA}$. The weak absorbers dominate our distribution. In Figure 2(c), we present the distribution of CIV $\lambda 1548$ rest-frame equivalent widths, W_r , of the detected absorbers for all redshifts ($1.0 \leq z \leq 4.75$), $z < 2.5$, and $z \geq 2.5$.

2.5. Redshift and Co-moving Path of the Survey

From the equivalent width detection limit mentioned in Section 2.3, we calculate the detection threshold of our survey. Namely, we construct the redshift path sensitivity function, $g(W_r, z)$ (e.g., Lanzetta et al. 1987), which is the number of quasars in which an absorber with rest-frame equivalent width W_r or greater could be detected at redshift z in our survey,

$$g(W_r, z) = \sum_q H(z - z_q^-) H(z_q^+ - z) H(W_r - 3\sigma_q(z)), \quad (1)$$

where $H(x)$ is the Heaviside step function, z_q^- , and z_q^+ are the minimum and maximum redshifts of the q^{th} quasar spectrum, respectively, and $\sigma_q(z)$ is the uncertainty in rest-frame equivalent width at redshift z in the q^{th} quasar spectrum. The sum extends over all quasars in the sample. We generate the $g(W_r, z)$ function for $W_{r,\text{lim}} \geq 0.005 \text{ \AA}$ over the range $z = 1$ to 5. The “heat map” shown in Figure 3 represents the number of quasar spectra in which a CIV $\lambda 1548, 1550$ feature with a given equivalent width or greater could be detected at the 3σ level at redshift z . The dark vertical bands around $z \sim 3.5$ and $z \sim 3.9$ represent excluded telluric bands at

6868–6932 Å and 7594–7700 Å, respectively. For a fixed W_r , the integral of $g(W_r, z)$ over a given redshift range

$$\Delta Z(W_r) = \int_{z_1}^{z_2} g(W_r, z) dz, \quad (2)$$

yields the redshift path over which absorbers with equivalent width W_r or greater could be detected in our survey at a 3σ significance level between z_1 and z_2 . Similarly, the “absorption distance”, which we will call the co-moving path, is defined as

$$\Delta X(W_r) = \int_{z_1}^{z_2} g(W_r, z) \frac{dX}{dz} dz \quad (3)$$

where

$$\frac{dX}{dz} = \frac{(1+z)^2}{\sqrt{\Omega_M(1+z)^3 + \Omega_\Lambda}} \quad (4)$$

accounts for both the radial and transverse components of the Hubble expansion. In the modern era of precision cosmology, the cosmological parameters Ω_M and Ω_Λ are known to a few percent accuracy (e.g., Komatsu et al. 2009), so that the function dX/dz is tightly constrained. As such, all analysis in this work will be conducted in terms of the co-moving path, as this allows any cosmic evolution in the absorber population to be directly measured (see Section 3.2 for details).

2.6. Survey Completeness and Science Sample

The survey detection sensitivity function is defined as the co-moving path over which an absorber with equivalent width W_r or greater could be detected in our survey normalized to the total co-moving path of the survey. In a given redshift range z_1 to z_2 , this function is

$$C(W_r) \Big|_{z_1}^{z_2} = \frac{\Delta X(W_r)}{\Delta X_{\max}}, \quad (5)$$

where $\Delta X(W_r)$ is computed from Eq. 3, and ΔX_{\max} , the total co-moving path of our survey, is computed from Eq. 3 with $g(W_r, z)$ calculated such that the Heaviside function $H(W_r - 3\sigma_q(z))$ in Eq. 1 is fixed at unity.

In Figure 4, we show selected survey detection sensitivity functions as a function of W_r . To a high approximation, this function is the 3σ detection completeness fraction for our survey. We divide our sample into the two redshift ranges, $1.0 \leq z < 2.5$ and $2.5 \leq z \leq 4.75$, because they have equal co-moving path coverage. Over our total redshift range, $1.0 \leq z \leq 4.75$, the survey is $\sim 50\%$ complete to $W_r = 0.05$ Å. The $1.0 \leq z < 2.5$ redshift interval reaches $\sim 50\%$ completeness at $W_r = 0.04$ Å, while the $2.5 \leq z \leq 4.75$ interval is $\sim 50\%$ complete at $W_r = 0.06$ Å. The survey is effectively 100% complete over all redshifts at $W_r = 0.3$ Å.

All subsequent analysis is restricted to CIV absorbers with $W_r \geq 0.05$ Å, which is the 50% completeness limit of the full redshift range of the survey. Applying this selection criterion, of the total 1625 CIV absorbers we located, we include 1318 CIV absorbers with $W_r \geq 0.05$ Å in our final science sample.

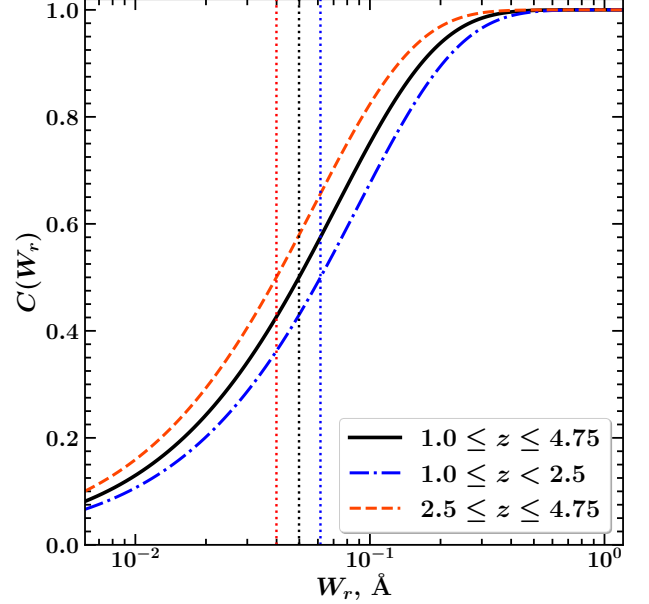


Figure 4. The 3σ detection threshold completeness, $C(W_r)$, as a function of rest-frame equivalent width. The black curve is $C(W_r)$ for the full redshift coverage of the survey. The dot-dashed blue curve shows $C(W_r)$ for redshifts $1.0 \leq z < 2.5$, while the dashed red curve shows $C(W_r)$ for $2.5 \leq z \leq 4.75$. The blue, red, and black vertical dotted lines represent the 50% completeness limits for $1.0 \leq z < 2.5$, $2.5 \leq z \leq 4.75$, and $1.0 \leq z \leq 4.75$, respectively.

3. RESULTS

3.1. Equivalent Width Distribution

We first characterized $n(W_r)$, the underlying (or true) equivalent width distribution (hereafter, EWD) of CIV absorbers. This is defined as the number of absorbers per unit equivalent width per unit co-moving path,

$$n(W_r) = \frac{d^2N}{dW_r dX}, \quad (6)$$

such that

$$\int_{W_{\min}}^{\infty} n(W_r) dW_r = \frac{dN}{dX}, \quad (7)$$

where dN/dX is the co-moving path density of absorbers with $W_r \geq W_{\min}$ (see Section 3.2). We are especially interested in the distribution when we account for the weak absorbers, i.e., those with $W_r < 0.3$ Å, as these have not been studied in previous investigations. We examined the CIV absorbers in equivalent width bins defined such that an equal number of absorbers is contained in each bin. The value of $n(W_r)$ in a bin centered on W_r between W_l and W_h is

$$n(W_l \leq W_r < W_h) = \frac{N(W_r)}{\Delta W_r \Delta X(W_r)}, \quad (8)$$

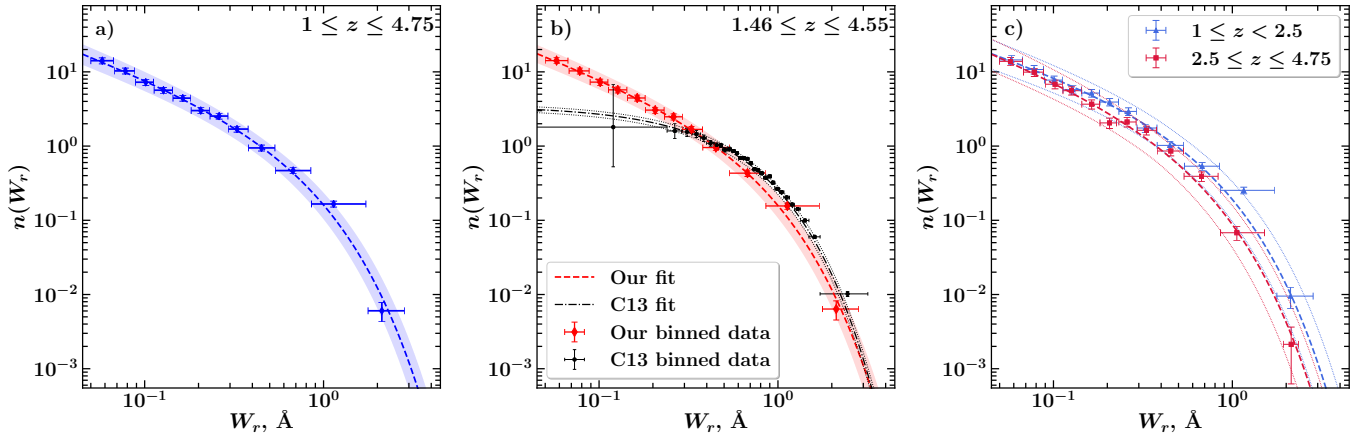


Figure 5. (a) The CIV $\lambda 1548$ equivalent width distribution, $n(W_r)$, for the full redshift range of our survey, $1.0 \leq z \leq 4.75$. The blue points show our observed $n(W_r)$ in W_r bins, the dashed blue curve shows the Schechter function fit to these binned data, and the shading represents the $\pm 1\sigma$ confidence interval for our fit. (b) Comparison of our $n(W_r)$ with that of C13 for C13’s redshift range: $1.46 \leq z \leq 4.55$. Red represents our data and fit; black points and error bars represent C13’s $n(W_r)$ and associated errors in each W_r bin, while the black curves show C13’s exponential fit to their data. (c) $n(W_r)$ for two different redshift ranges, $1.0 \leq z < 2.5$ (blue) and $2.5 \leq z \leq 4.75$ (red), with the best-fit Schechter functions shown by dashed curves and the $\pm 1\sigma$ uncertainties shown by dotted curves. All of our fit parameters are presented in Table 3.

where $N(W_r)$ is the number of absorbers in the bin, $\Delta W_r = W_h - W_l$ is the bin width, and the quantity $\Delta X(W_r) = [\Delta X(W_l) + \Delta X(W_h)]/2$ is the averaged total co-moving path length available for the bin as computed using Eq. 3.

We present the observed EWD, for different ranges, in Figures 5(a)–(c). The fitted data points are $(\overline{W}_r, n(W_r))$, where \overline{W}_r is the mean equivalent width of absorbers in the bin and $n(W_r)$ is given by Eq. 8. The uncertainties in \overline{W}_r are the standard deviations of the equivalent widths of the absorbers in the bin. We adopt the standard deviations as a true reflection of the distribution of values inside the bin, rather than the bin width ΔW_r , which would over-estimate the distribution of points in the bin. The uncertainties in $n(W_r)$ are obtained assuming Poisson fluctuations; there are roughly 100 absorbers per binned data point.

To explore any difference in the EWD with redshift, we fit the EWD for $1.0 \leq z \leq 4.75$ (the full survey range; Figure 5(a)), and for $1.0 \leq z < 2.5$ and $2.5 \leq z \leq 4.75$ (Figure 5(c)), which each have equal total co-moving path lengths, ΔX , for $W_r \geq 0.05 \text{ \AA}$. We also fit the EWD over $1.46 \leq z \leq 4.55$ in order to directly compare our EWD with that of C13 over their redshift range (Figure 5(b)).

The shape of our observed EWD indicates a slow power-law decline with W_r at the weak end and a rapid exponential decline at the strong end of the frequency distribution. This is not unexpected, as sensitive high-resolution surveys that probe down to the linear part of the curve of growth found power-law distributions for the column density (e.g., Songaila 2001, 2005; D’Odorico et al. 2010; Boksenberg & Sargent 2015), whereas larger

surveys sensitive to $W_r \geq 0.3 \text{ \AA}$ reported an exponential distribution for equivalent widths (e.g., Sargent et al. 1988; Cooksey et al. 2010, C13). Thus, following the parameterization of Kacprzak & Churchill (2011) of the distribution of strong and weak MgII absorbers, we fit the observed CIV EWD by a Schechter (1976) function

$$n(W_r) dW_r = n_* \left(\frac{W_r}{W_*} \right)^\alpha \exp \left(-\frac{W_r}{W_*} \right) dW_r, \quad (9)$$

where α is the weak-end power-law slope, W_* is the characteristic equivalent width where the function transitions from a power-law to an exponential function, and n_* is the normalization.

We obtained best-fit values for n_* , W_* , and α , using the least-squares orthogonal distance regression (ODR) method in the SCIPY package,³ which accounts for uncertainties in both the dependent and independent variables. We use the ODR method for all subsequent functional fits in this paper.

Before adopting our final best-fit parameters, we perform a series of experiments to explore sensitivity to the number of bins used in the least-squares fit. We fit the data using 10, 11, 12, 13, and 14 bins, while always enforcing an equal number of absorbers in each bin. We also explored the use of 1σ and 3σ uncertainties in the binned W_r , $n(W_r)$ ordered pairs. The fitted parameters n_* , W_* , and α are found to be highly robust against changes in the number of bins and the use of 1σ or 3σ uncertainties, meaning that variations in the values of the best-fit parameters are within the $\pm 1\sigma$ uncertainties for all experiments. The 12 bin fit yielded the

³ <https://docs.scipy.org/doc/scipy/reference/odr.html>

smallest fitted-parameter uncertainties, whereas the 10 and 11 bin fits yielded the largest. The adopted best-fit Schechter function parameters were obtained by computing the 1σ variance-weighted means of the 10, 11, 12, 13, and 14 bin experiments. These best-fit parameters are listed in Table 3. Note that n_* is the most uncertain fitted parameter, while W_* and α are better constrained.

Table 3. EWD Fit Parameters (see Figure 5)

z_1	z_2	α	W_* (Å)	n_* (Å ⁻¹)
1.00	4.75	-0.91 ± 0.04	0.52 ± 0.04	2.05 ± 0.30
1.46 ^a	4.55 ^a	-0.91 ± 0.03	0.50 ± 0.04	2.13 ± 0.28
1.00	2.50	-0.82 ± 0.06	0.48 ± 0.06	2.79 ± 0.58
2.50	4.75	-0.98 ± 0.07	0.42 ± 0.05	2.14 ± 0.48

^aThe redshift range of C13, for comparison.

In Figure 5(a), we present the best-fit Schechter function for the full redshift range of our sample, $1.0 \leq z \leq 4.75$. The shaded region represents the $\pm 1\sigma$ confidence interval given the uncertainties in the three fitted parameters. In Figure 5(b), we compare our EWD to that of C13 over the redshift range of their sample, $1.46 \leq z \leq 4.55$. The C13 distribution is fit well by an exponential function, but their sample is only $\sim 20\%$ complete at $W_r = 0.3$ Å. Our sample is 50% complete at $W_r = 0.05$ Å and is well-fit to a Schechter function. Note that the power-law portion of the Schechter function is clearly established for $W_r \leq 0.3$ Å. For both $1.0 \leq z \leq 4.75$ and $1.46 \leq z \leq 4.55$, we obtain virtually identical Schechter parameters: $\alpha \simeq -0.9$, $W_* \simeq 0.5$ Å, and $n_* \simeq 2.1$.

In Figure 5(c), we present the EWDs for two redshift ranges, $1 \leq z < 2.5$ and $2.5 \leq z \leq 4.75$, chosen such that both redshift ranges have equal survey co-moving path lengths. Our data indicate a steeper weak-end power-law slope at higher redshift, $\alpha \simeq -1$, than at lower redshift, $\alpha \simeq -0.8$. At higher redshift, we also find that the normalization, n_* , decreases by $\sim 20\%$, and the characteristic transition from a power-law to exponential distribution, W_* , falls by $\sim 10\%$. Taken together, these best fit parameters indicate redshift evolution in the relative frequencies of weaker and stronger absorbers; at higher redshifts, the frequency of weaker absorbers relative to stronger absorbers is higher than at lower redshifts.

3.2. Co-moving Path Density, dN/dX

For a given population of absorbers, the observed co-moving path density is proportional to the product of the absorber cosmic number density, $n(z)$, and the absorbing structure physical cross-section, $\sigma(z)$,

$$\frac{dN(z)}{dX} \equiv N_x(z) = \frac{c}{H_0} n(z)\sigma(z), \quad (10)$$

where we hereafter adopt $N_x(z)$ to designate the *measured value* of co-moving path density. Examination of $dN(z)/dX$ provides direct insights into the redshift evolution of the product $n(z)\sigma(z)$; a non-evolving population of absorbers will have a constant co-moving path density as a function of redshift.

Historically, it was the redshift path density, dN/dz , that has been employed to measure the cosmic evolution of a population of absorber, where dN/dz is defined as the observed number of absorbers with equivalent width W_r or greater per unit of redshift (e.g. Sargent et al. 1988; Steidel 1990; Misawa et al. 2002; Péroux et al. 2004). The co-moving path density is related to dN/dz through the relation

$$\frac{dN(z)}{dz} = \frac{dN(z)}{dX} \frac{dX}{dz}, \quad (11)$$

where the function dX/dz is defined in Eq. 4. Unlike dN/dX , dN/dz is not a constant for a non-evolving population of absorbers. Thus, we use dN/dX to characterize the evolution of CIV absorbers rather than dN/dz .

We examined the co-moving path density as a function of both redshift and equivalent width. In a given redshift range spanning z_1 to z_2 , the co-moving path density and its variance are obtained by summing over all N_{abs} absorbers in the redshift range whose rest-frame equivalent widths are greater than or equal to $W_{r,\text{lim}}$. Thus, we measure N_x as

$$N_x(W_i \geq W_{r,\text{lim}}) \Big|_{z_1}^{z_2} = \sum_{i=1}^{N_{\text{abs}}} \frac{1}{\Delta X(W_i)}, \quad (12)$$

$$\sigma_{N_x}^2(W_i \geq W_{r,\text{lim}}) \Big|_{z_1}^{z_2} = \sum_{i=1}^{N_{\text{abs}}} \left[\frac{1}{\Delta X(W_i)} \right]^2.$$

where $\Delta X(W_i)$, as computed using Eq. 3, is the total co-moving path over which absorber i with rest-frame equivalent width W_i could be detected at the 3σ significance level accounting for all quasars in the survey.

In applying Eq. 12, we resolve redshift into bins (z_1, z_2] such that an equal number of absorbers reside in each bin for the minimum equivalent width threshold $W_{r,\text{lim}} = 0.05$ Å. We use 10 redshift bins, each of which has ~ 130 absorbers. These redshift bins are also adopted for the $W_{r,\text{lim}} = 0.3$ Å and $W_{r,\text{lim}} = 0.6$ Å populations. In Figure 6, we present the observed $N_x(z)$ over the redshift range $1.0 \leq z \leq 4.75$ for three minimum equivalent width thresholds, $W_{r,\text{lim}} = 0.05$ Å, 0.3 Å, and 0.6 Å. We list our observed $N_x(z)$ values in Table 4. For comparison, we also present $N_x(z)$ values from C13 for $W_{r,\text{lim}} = 0.6$ Å for the redshift range $1.46 \leq z \leq 4.55$; our values are consistent with those of C13, who were $\sim 50\%$ complete at $W_r \simeq 0.6$ Å.

Examination of Figure 6 clearly shows two types of evolution. First, for all three equivalent width thresholds, the co-moving path density decreases with increasing redshift. Second, this evolution is more pronounced

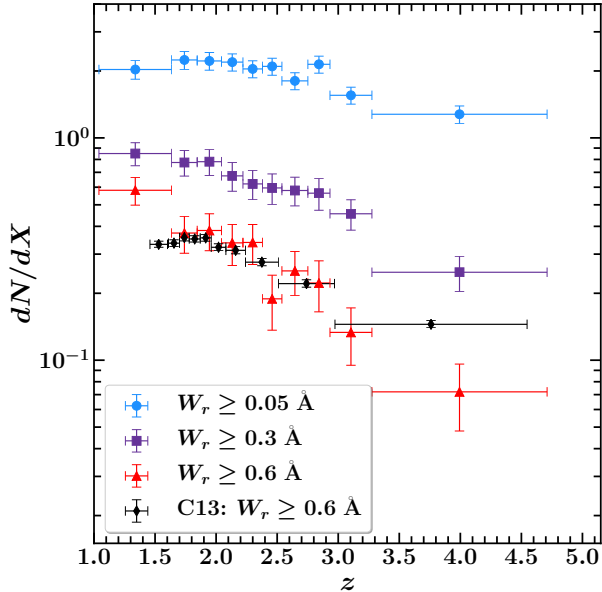


Figure 6. The measured CIV absorber co-moving path density $N_x(z) = dN/dX$ as a function of redshift for the rest-frame equivalent width thresholds of 0.05 Å (light blue circles), 0.3 Å (purple squares), and 0.6 Å (red triangles), and associated errors. For comparison, we show $N_x(z)$ for $W_r \geq 0.6$ Å from C13 (black diamond points). Our measured values are presented in Table 4.

Table 4. Measured Co-moving Path Density (see Figure 6)

$\langle z \rangle$	Δz^a	$N_x(z)$ ($W_r \geq 0.05$ Å)	$N_x(z)$ ($W_r \geq 0.3$ Å)	$N_x(z)$ ($W_r \geq 0.6$ Å)
1.338	0.595	2.02 ± 0.19	0.84 ± 0.10	0.57 ± 0.08
1.738	0.206	2.29 ± 0.21	0.81 ± 0.11	0.40 ± 0.07
1.942	0.202	2.16 ± 0.20	0.75 ± 0.10	0.36 ± 0.07
2.131	0.176	2.16 ± 0.19	0.69 ± 0.10	0.35 ± 0.07
2.298	0.157	2.10 ± 0.18	0.64 ± 0.10	0.35 ± 0.07
2.456	0.159	2.09 ± 0.18	0.61 ± 0.09	0.20 ± 0.05
2.640	0.209	1.78 ± 0.16	0.58 ± 0.09	0.25 ± 0.06
2.837	0.185	2.06 ± 0.18	0.55 ± 0.09	0.22 ± 0.06
3.100	0.341	1.57 ± 0.14	0.46 ± 0.07	0.13 ± 0.04
3.990	1.440	1.24 ± 0.11	0.25 ± 0.04	0.07 ± 0.02

^aThe redshift bins, $\Delta z = z_2 - z_1$ with $\langle z \rangle = (z_1 + z_2)/2$, are defined such that the $W_{r,\text{lim}} = 0.05$ Å sample has equal numbers of absorbers in each bin.

as the equivalent width threshold is increased. The ratio of $N_x(z)$ of the $W_{r,\text{lim}} = 0.05$ Å sample to the $W_{r,\text{lim}} = 0.6$ Å sample changes from ~ 3.5 at $\langle z \rangle = 1.3$ to ~ 18 at $\langle z \rangle = 4$.

From Eq. 10, we infer that the product of cosmic number density and absorber cross-section, $n(z)\sigma(z)$, increases for all of the populations of absorbers we study at $1.0 \leq z \leq 4.75$, with the increase being more rapid for

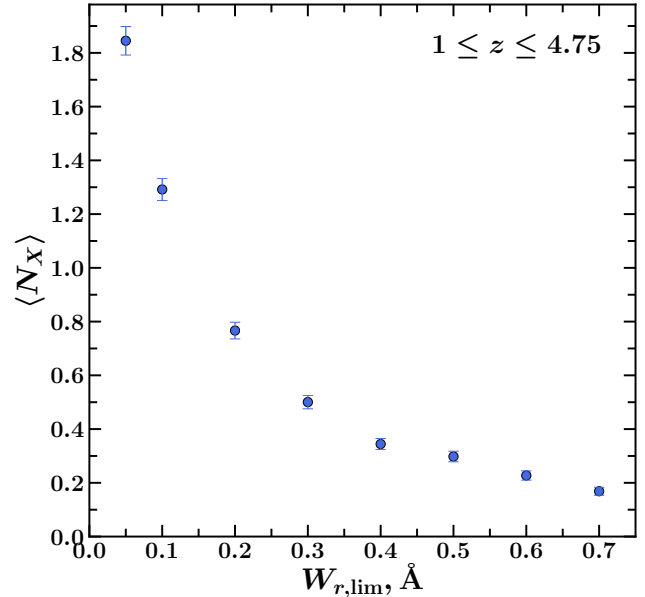


Figure 7. The observed cosmic mean co-moving path density of CIV absorbers, $\langle N_x \rangle = (c/H_0)\langle n\sigma \rangle$, over the redshift range $1.0 \leq z \leq 4.75$ as a function $W_{r,\text{lim}}$.

absorbers with larger W_r . For the absorbers defined by $W_r \geq 0.05$ Å, a shallow rise in $N_x(z)$ of a factor of $\simeq 1.8$ is observed. The co-moving path density for $W_r \geq 0.3$ Å absorbers rises by a factor of $\simeq 3.3$ over this period. For absorbers with $W_r \geq 0.6$ Å, the co-moving path density increases by a factor of $\simeq 8.1$ over this period, which is $\simeq 2.5$ times the rise for $W_r \geq 0.3$ Å absorbers and $\simeq 4.5$ times the rise for $W_r \geq 0.05$ Å absorbers. These results reinforce our finding that the EWD is evolving such that at higher redshifts there are relatively more weak absorbers to strong absorbers than there are at lower redshifts (also see Figure 5).

To further characterize the incidence of CIV absorbers, we define the measured cosmic mean co-moving path density

$$\langle N_x \rangle = \frac{c}{H_0} \langle n\sigma \rangle, \quad (13)$$

as the arithmetic mean of the measured $N_x(z)$ of an absorber population, weighted by the variance within each redshift bin, in the redshift range $1.0 \leq z \leq 4.75$. In Figure 7, we show $\langle N_x \rangle$ over the redshift range $1.0 \leq z \leq 4.75$ as a function $W_{r,\text{lim}}$. Over this redshift range, we see that the cosmic mean co-moving path density decreases as $W_{r,\text{lim}}$ increases; the mean incidence of the weakest absorbers with $W_r \geq 0.05$ Å is almost an order of magnitude higher than the strongest absorbers we studied, with $W_r \geq 0.7$ Å.

3.3. Quantifying Evolution

We aim to further quantify the evolutionary characteristics in $N_x(z)$, and therefore the product $n(z)\sigma(z)$, by examining redshift evolution as a function of mini-

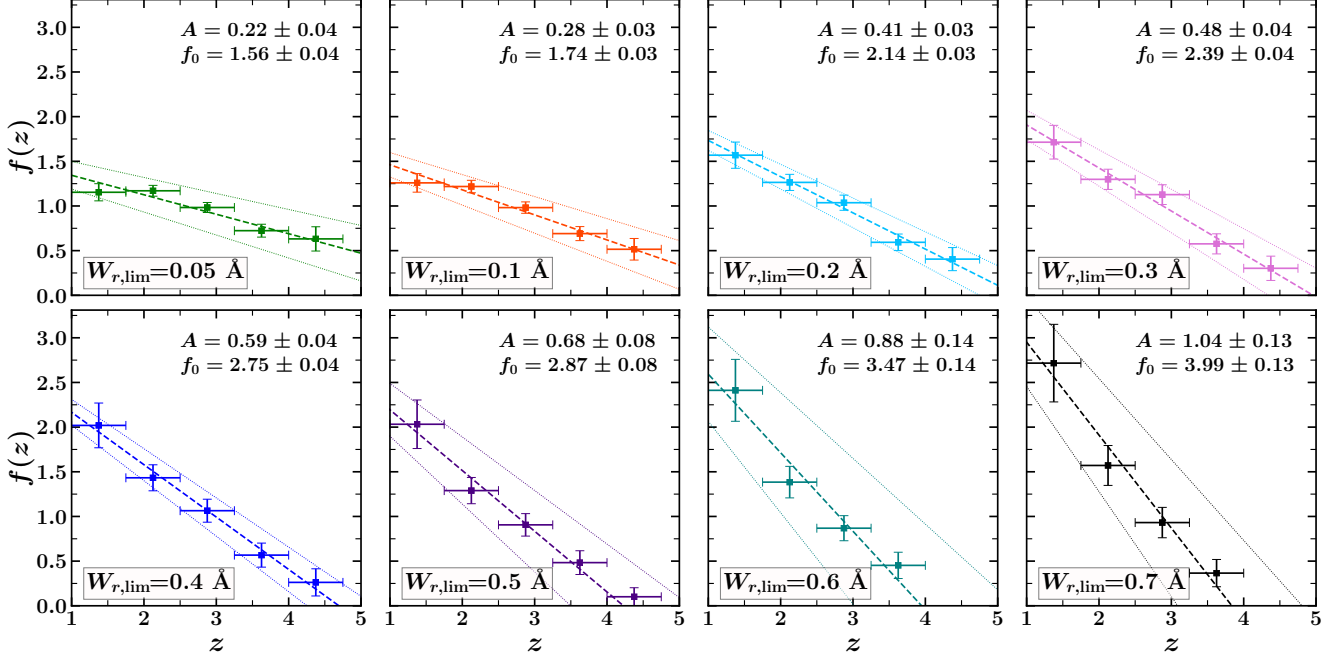


Figure 8. The observed ratio $f(z) = N_x(z)/\langle N_x \rangle$ is plotted as a function of redshift for subsamples having differing minimum rest-frame equivalent widths. The dashed lines through the data are the least-squares fits to Eq. 15, with the dotted lines representing the $\pm 1\sigma$ confidence intervals. The individual panels are for absorber populations defined by (a) $W_{r,\text{lim}} = 0.05 \text{ \AA}$, (b) $W_{r,\text{lim}} = 0.1 \text{ \AA}$, (c) $W_{r,\text{lim}} = 0.2 \text{ \AA}$, (d) $W_{r,\text{lim}} = 0.3 \text{ \AA}$, (e) $W_{r,\text{lim}} = 0.4 \text{ \AA}$, (f) $W_{r,\text{lim}} = 0.5 \text{ \AA}$, (g) $W_{r,\text{lim}} = 0.6 \text{ \AA}$, (h) $W_{r,\text{lim}} = 0.7 \text{ \AA}$.

imum equivalent width threshold, $W_{r,\text{lim}}$. We examine the ratio

$$\frac{N_x(z)}{\langle N_x \rangle} = \frac{n(z)\sigma(z)}{\langle n\sigma \rangle} = f(z), \quad (14)$$

which we can parameterize with an arbitrary function of redshift, $f(z)$. We considered five equal redshift bins of $\Delta z = 0.75$ in the range $1.0 \leq z \leq 4.75$, for absorber populations with $W_{r,\text{lim}} = 0.05 \text{ \AA}$ and with $W_{r,\text{lim}} = 0.1 \text{ \AA}$ to 0.7 \AA , in steps of 0.1 \AA .

Based on the evolution exhibited in Figure 6, we adopted a simple first-order polynomial for $f(z)$,

$$f(z) = f_0 - Az, \quad (15)$$

where $f_0 = f(z=0)$ and $A = -df(z)/dz$ is the slope, which gives the negative of the rate of change.

If we are to equate a physical meaning to the model parameters, we would interpret A as an “evolution constant” describing the evolution rate of the ratio $n(z)\sigma(z)/\langle n\sigma \rangle$ over the redshift range $1.0 \leq z \leq 4.75$. For the zero intercept, f_0 , we would interpret this as the ratio of the present-epoch ($z = 0$) product $n_0\sigma_0 = n(0)\sigma(0)$, to the measured cosmic mean, $\langle n\sigma \rangle$. Our model also yields a derived quantity, which is the redshift above which the incidence of absorbers in our survey vanishes, i.e., $f(z_0) = 0$, which corresponds to $z_0 = f_0/A$. We would interpret z_0 as an “onset redshift”, meaning the redshift at which the absorber population

would first appear in the universe. Both f_0 and z_0 are based on linear extrapolation of the model, which is fit only in the redshift range $1.0 \leq z \leq 4.75$.

We computed $f(z) = N_x/\langle N_x \rangle$ in each redshift bin, for each $W_{r,\text{lim}}$ threshold. The results are presented in Figures 8(a)–(h). We performed a least-squares fit using ODR to Eq. 15 for each $W_{r,\text{lim}}$ sample and obtained the best-fit parameters f_0 and A and their uncertainties. The fitted functions are superimposed on the data in Figures 8(a)–(h). The fitted parameters and the onset redshift, z_0 , are listed in Table 5. The positive evolution constant indicates that the product $n(z)\sigma(z)$ is increasing with cosmic time (decreasing with redshift).

Figures 8(a)–(h) show that the data are well-described by a linear evolution with redshift for all populations of absorbers, with the rate of evolution being more rapid for larger $W_{r,\text{lim}}$. The positive evolution constant for all $W_{r,\text{lim}}$ indicates that the product $n(z)\sigma(z)$ is increasing with cosmic time for all populations of CIV absorbers.

In Figure 9(a), we plot the evolution constant as a function of $W_{r,\text{lim}}$. With the progression of cosmic time, the ratio $A = n(z)\sigma(z)/\langle n\sigma \rangle$ increases by a factor of $\sim 25\%$ per unit redshift for $W_{r,\text{lim}} = 0.1 \text{ \AA}$, whereas this quantity increases by a factor of $\sim 100\%$ per unit redshift for $W_{r,\text{lim}} = 0.7 \text{ \AA}$. Thus, the product $n(z)\sigma(z)$ of the larger W_r absorbers rises much faster than that of the smaller W_r absorbers.

In Figure 9(b), we plot $f_0 = n_0\sigma_0/\langle n\sigma \rangle$ as a function

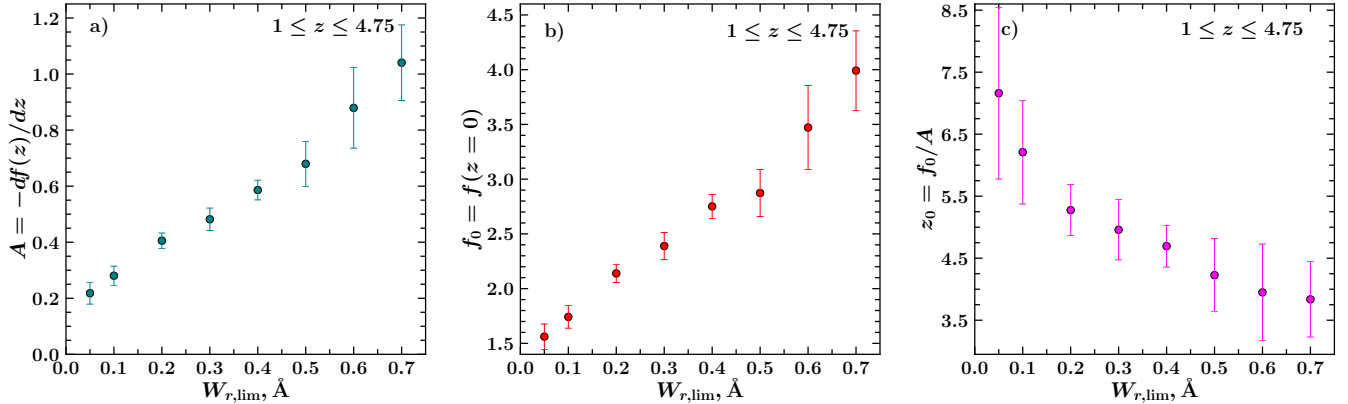


Figure 9. (a) The best-fit parameter $A = -df(z)/dz$, which we call the evolution constant. This is the rate of evolution of the product $n(z)\sigma(z)$ per unit redshift for CIV absorbers having $W_r \geq W_{r,\text{lim}}$. A increases linearly with $W_{r,\text{lim}}$. (b) The best-fit parameter $f_0 = N_X(z=0)/\langle N_X \rangle$, which is the ratio of the product of the present-epoch $n_0\sigma_0$ to the measured cosmic mean value $\langle n\sigma \rangle$ for a given $W_{r,\text{lim}}$. Under the assumption that evolution remains linear from $z=1$ to $z=0$, this ratio is predicted to increase in direct proportion to $W_{r,\text{lim}}$. (c) The best-fit parameter $z_0 = f_0/A$, which is the onset redshift for CIV absorbers having $W_r \geq W_{r,\text{lim}}$. The onset redshift decreases monotonically with increasing $W_{r,\text{lim}}$, following $z_0 \propto W_{r,\text{lim}}^{-0.22}$.

Table 5. Best-Fit Evolution Model Parameters

$W_{r,\text{lim}}$ (\AA)	$\langle N_X \rangle$	A	f_0	z_0
0.05	1.85 ± 0.05	0.22 ± 0.04	1.56 ± 0.12	7.16 ± 1.39
0.1	1.29 ± 0.04	0.28 ± 0.03	1.74 ± 0.10	6.21 ± 0.84
0.2	0.77 ± 0.03	0.41 ± 0.03	2.14 ± 0.08	5.28 ± 0.41
0.3	0.50 ± 0.02	0.48 ± 0.04	2.39 ± 0.12	4.96 ± 0.49
0.4	0.34 ± 0.02	0.59 ± 0.04	2.75 ± 0.11	4.69 ± 0.34
0.5	0.30 ± 0.02	0.68 ± 0.08	2.87 ± 0.22	4.23 ± 0.59
0.6	0.23 ± 0.02	0.88 ± 0.14	3.47 ± 0.38	3.95 ± 0.78
0.7	0.17 ± 0.01	1.04 ± 0.13	3.99 ± 0.36	3.84 ± 0.61

of $W_{r,\text{lim}}$. As the minimum redshift of our survey is $z=1.0$, the value of f_0 has physical meaning only under the assumption that $f(z)$ can be linearly extrapolated to $z=0$. Assuming linear evolution continues to $z=0$ (over the last $\simeq 7.7$ Gyr of cosmic time), our model would suggest $n_0\sigma_0/\langle n\sigma \rangle$ is a factor of ~ 1.6 for $W_{r,\text{lim}} = 0.05 \text{ \AA}$ and increases to ~ 4.0 for $W_{r,\text{lim}} = 0.6 \text{ \AA}$. We investigate how well the extrapolations for the $W_{r,\text{lim}} = 0.05 \text{ \AA}$ and $W_{r,\text{lim}} = 0.6 \text{ \AA}$ populations hold up against the observed $z < 1$ data from the literature in Section 4.3.

In Figure 9(c), we plot the onset redshift, $z_0 = f_0/A$, as a function of $W_{r,\text{lim}}$. For example, our simple model would suggest that CIV absorbers with $W_{r,\text{lim}} = 0.6 \text{ \AA}$ should have a cosmic onset in the approximate redshift range $3.2 \leq z \leq 4.7$. Accounting for uncertainties in the extrapolation to obtain z_0 , the onset redshifts for $W_{r,\text{lim}} \leq 0.4 \text{ \AA}$ populations are above $z = 4.75$, which are greater than the maximum redshift of our survey. Thus, for the $W_{r,\text{lim}} < 0.4 \text{ \AA}$ absorber populations, z_0

is a valid quantity only under the condition that linear evolution of the absorber populations continues beyond the redshift range of our model fits.

As $W_{r,\text{lim}}$ of the population is lowered, extrapolation yields onset redshifts that increase such that absorbers with $W_{r,\text{lim}} = 0.3 \text{ \AA}$ would not be present above $z \sim 5.5$ and absorbers with $W_{r,\text{lim}} = 0.05 \text{ \AA}$ would not be present above $z \sim 8.6$. The uncertainties in these predicted onset redshifts increase with decreasing $W_{r,\text{lim}}$. However, given our simple linear model, allowing for cosmic variance, and considering that we have no *a priori* expectation for linear evolution to hold for $z > 4.75$, we reserve further judgement as to any predictive features of the linear model. In Section 4.3, we contrast expectations of the model at higher redshifts with the available data in the literature, and in Section 4.6, compare both the model and the data to cosmological simulations.

Table 6. Model Parameters Fits

Parameterization	a	b
$\langle N_X \rangle = aW^{-b}$	0.17 ± 0.02	0.83 ± 0.05
$z_0 = aW^{-b}$	3.71 ± 0.09	0.23 ± 0.02
$A = aW + b$	1.08 ± 0.06	0.17 ± 0.02
$f_0 = aW + b$	3.32 ± 0.17	1.42 ± 0.05

NOTE— W represents $W_{r,\text{lim}}$. Fits are applicable for $W_{r,\text{lim}} = 0.05 \text{ \AA}$ to 0.7 \AA over the redshift range $1.0 \leq z \leq 4.75$.

As a guide to the behavior of our fitting parameters as a function of $W_{r,\text{lim}}$, we performed least squares fits to $\langle N_X \rangle$ (see Figure 7), A , f_0 , and z_0 (see Figure 9). The convenient functional forms of these parameters are presented in Table 6. Both $\langle N_X \rangle$ and z_0 are well

fit by a declining power law, whereas A and f_0 increase linearly with $W_{r,\text{lim}}$.

4. DISCUSSION

This survey has provided a first opportunity to examine the properties of a sizable sample of “weak” ($W_r \leq 0.3 \text{ \AA}$) CIV absorbers over the redshift range $1.0 \leq z \leq 4.75$, which corresponds to a cosmic time from when the universe was ~ 1.5 Gyr old ($z = 4.75$) to when it was ~ 6 Gyr old ($z = 1.0$). Thus, we explore the evolutionary behavior of CIV absorption-selected gas structures for a ~ 4.5 Gyr period corresponding to $\sim 10\%$ to $\sim 45\%$ of the present age of the universe. With this work, we (1) extended previous measurements of the EWD and dN/dX by an order of magnitude, down to $W_{r,\text{lim}} = 0.05 \text{ \AA}$, and (2) characterized redshift evolution in dN/dX as a function of equivalent width threshold over three orders of magnitude in W_r .

4.1. CIV Evolution Across $1.0 \leq z \leq 4.75$

In a pioneering survey, Sargent et al. (1988) found that the redshift path density, dN/dz , of strong ($W_r \geq 0.3 \text{ \AA}$) absorbers increased by a factor of roughly three from $z \sim 3.4$ to $z \sim 1.3$. Extending their sample, Steidel (1990) reported this increase to be a factor of roughly four at $1.3 \leq z \leq 4$. The trend of increasing redshift path density with cosmic time for strong absorbers was later confirmed by Misawa et al. (2002) ($2.3 \leq z \leq 4.5$) and Péroux et al. (2004) ($1.5 \leq z \leq 4.5$). For $W_r \geq 0.3 \text{ \AA}$, C13 found a factor of $\simeq 2.5$ increase in dN/dX from $z = 4.55$ to $z = 2$ followed by a plateau at $z \leq 2$ (they had only $\sim 20\%$ completeness at $W_r = 0.3 \text{ \AA}$). Similar to these previous works, we found $W_r \geq 0.3 \text{ \AA}$ absorbers increase monotonically by a factor of roughly three over this same cosmic period, with no sign of a plateau for $z \leq 2$ (we are $\sim 100\%$ complete at $W_r = 0.3 \text{ \AA}$).

As reproduced in Figure 6, C13 found that dN/dX of $W_r \geq 0.6 \text{ \AA}$ absorbers increases by a factor of roughly 2.5 from $z = 4.55$ to $z = 2$ and then are consistent with no evolution or a shallow decline from $z \sim 2$ to $z \sim 1.5$. Our measured dN/dX for $W_{r,\text{lim}} = 0.6 \text{ \AA}$ is consistent with that of C13 in the range $1.6 \leq z \leq 3.3$, but is roughly ~ 2.1 times lower for $3.4 \leq z \leq 4.5$. For this population of absorbers, we found that dN/dX increases monotonically and smoothly by a factor of roughly eight from $z = 4.75$ to $z = 1$.

The new insights into CIV evolution from this work are that CIV absorbers are evolving linearly with redshift over the ~ 4.5 Gyr time period from $z = 4.75$ to $z = 1$, such that the rate of evolution is dependent on the strength of absorption. The higher the $W_{r,\text{lim}}$ of the absorber population, the steeper the linear increase in dN/dX with decreasing redshift. This quantifiable “differential cosmic evolution” with equivalent width threshold is informing us how the product $n(z)\sigma(z)$ is evolving as a function of the absorbing gas optical depth and ve-

locity profile. We discuss physical interpretations of the observed evolution in Section 4.5.

4.2. Modeling CIV Evolution

The inverse-power law (asymptotic) decline in $\langle N_x \rangle$ with increasing $W_{r,\text{lim}}$ suggests that the cosmic mean $\langle n\sigma \rangle$ across $1.0 \leq z \leq 4.75$ is smaller for populations of absorbers with progressively higher equivalent widths. In part, this behavior is reflecting the general behavior of the EWD across all redshifts, that smaller W_r absorbers are more common than larger W_r absorbers. For a given $W_{r,\text{lim}}$, the linear decline in $N_x(z)/\langle N_x \rangle$ with redshift is either due to evolution in the number density, $n(z)$, the statistical absorber cross-section, $\sigma(z)$, or some combination of both. The next level of detail in understanding CIV absorber evolution will consist of better understanding the evolution in $n(z)\sigma(z)$ for each absorber population. The linear model we have formulated can, in principle, be applied to constrain the nature of this evolution.

Consider the evolution of the $W_{r,\text{lim}} = 0.6 \text{ \AA}$ population. From Table 5, which gives $A \simeq 0.9$, we infer that the dimensionless ratio $n(z)\sigma(z)/\langle n\sigma \rangle$ decreases by 90% for each unit of redshift. Since $\langle n\sigma \rangle = (H_0/c)\langle N_x \rangle$, the evolution can be expressed in physical units. For $W_{r,\text{lim}} = 0.6 \text{ \AA}$, we measured $\langle N_x \rangle = 0.23$, which yields $\langle n\sigma \rangle \simeq 0.055 \text{ kpc}^{-1}$. Multiplying by the evolution constant, we obtain the physical evolution rate, $\mathcal{A} = \langle n\sigma \rangle A = (0.055) \cdot (0.9) = 0.05 \text{ kpc}^{-1}$ per unit redshift.

The physical evolution rate has the potential to provide powerful constraints on the absorber evolution. Adopting the definition $\mathcal{A} = \langle n\sigma \rangle A = -d[n(z)\sigma(z)]/dz$, we have

$$\mathcal{A} = -n(z)\frac{d\sigma(z)}{dz} - \sigma(z)\frac{dn(z)}{dz}. \quad (16)$$

Quantifying each term in this equation, $n(z)$, $dn(z)/dz$, $\sigma(z)$, and $d\sigma(z)/dz$, as a function of $W_{r,\text{lim}}$, would completely specify the statistical evolution of CIV absorbers. This would require extensive modeling, which would draw on a broader set of observational constraints to inform the model. State-of-the-art theoretical simulations hold the key to addressing the physics underlying the evolution in $n(z)$ and $\sigma(z)$ and how they manifest the observed evolution of CIV absorbing structures.

4.3. CIV Evolution Across ~ 12 Gyr

In order to construct a broader picture of CIV evolution from the first ~ 1 Gyr after the big bang ($z \sim 6$) to the present day ($z = 0$) and compare to the simple linear extrapolations of our evolution model, we searched the literature for observations of dN/dX in the redshifts $z < 1$ and $z > 4.75$.

There are caveats associated with comparing comoving path densities from the literature. The lower

the spectral resolution of a survey, the less sensitivity it has to lower W_r absorbers and the more rapidly the survey incompleteness grows as $W_{r,\text{lim}}$ is decreased. High-resolution surveys, on the other hand, can be sensitive to much smaller W_r . However, low-resolution surveys often comprise vastly greater numbers of quasar spectra (and therefore total redshift path coverage) than high-resolution surveys. This results in generally smaller uncertainties in the dN/dX measurements of low-resolution surveys and large enough redshift path length coverage to accurately sample the larger W_r absorbers, which are rarer due to the exponential drop in the EWD. Because of the typically shorter total redshift path coverage of high-resolution surveys, they can suffer from Poisson noise in the counts of the highest W_r absorbers.

Additional subtleties include the definition of the search space. C13 restrict their absorbers to those blueshifted by $\Delta v_{\text{QSO}} > 5000 \text{ km s}^{-1}$ from the quasar emission redshift in order to exclude absorbers intrinsic to the quasar environment, while we used a slightly less stringent cut-off of $\Delta v_{\text{QSO}} > 3000 \text{ km s}^{-1}$. Fortunately, C13 determined that changing from $\Delta v_{\text{QSO}} > 3000 \text{ km s}^{-1}$ to $\Delta v_{\text{QSO}} > 5000 \text{ km s}^{-1}$ affects their measured dN/dX by no more than 2%, which is much smaller than our uncertainties.

Furthermore, in higher resolution spectra, the definition of what constitutes a single CIV absorber can vary from study to study. For instance, D’Odorico et al. (2013) defined absorbers within a $\Delta v = \pm 50 \text{ km s}^{-1}$ velocity window, whereas we used $\Delta v = \pm 500 \text{ km s}^{-1}$. Moreover, some studies use equivalent width as a fundamental measurement to define an absorber population (e.g., Sargent et al. 1988; Steidel 1990), whereas others use column density (e.g., D’Odorico et al. 2013; Burchett et al. 2015; Codoreanu et al. 2018). Finally, how one determines their survey completeness in order to apply redshift path corrections as a function of $W_{r,\text{lim}}$ or column density threshold is central to measuring dN/dX .

From our literature search, we found measurements of dN/dX that extend to both $z < 1$ and $z > 4.75$ for only the $W_r \geq 0.05 \text{ \AA}$ and $W_r \geq 0.6 \text{ \AA}$ populations. For $z < 1$, we found $W_r \geq 0.05 \text{ \AA}$ measurements from Cooksey et al. (2010) and Burchett et al. (2015) and $W_r \geq 0.6 \text{ \AA}$ measurements from Cooksey et al. (2010). For $z > 4.75$, we obtained $W_r \geq 0.05 \text{ \AA}$ measurements from Codoreanu et al. (2018)⁴ and $W_r \geq 0.6 \text{ \AA}$ measurements from Simcoe et al. (2011). These data thus provide a comparison over the full redshift range $z \sim 0$ to $z \sim 6$ and enable us to assess the validity of our linear evolution model in the first 0.9 – 1.5 Gyr and last ~ 7.7 Gyr of cosmic time for these two CIV absorber populations.

⁴ Codoreanu et al. (2018) note that their own measured values of dN/dX and dN/dz roughly agree with the value they estimated from the $z \gtrsim 5$ high-resolution sample published by D’Odorico et al. (2013), who did not compute dN/dX nor dN/dz .

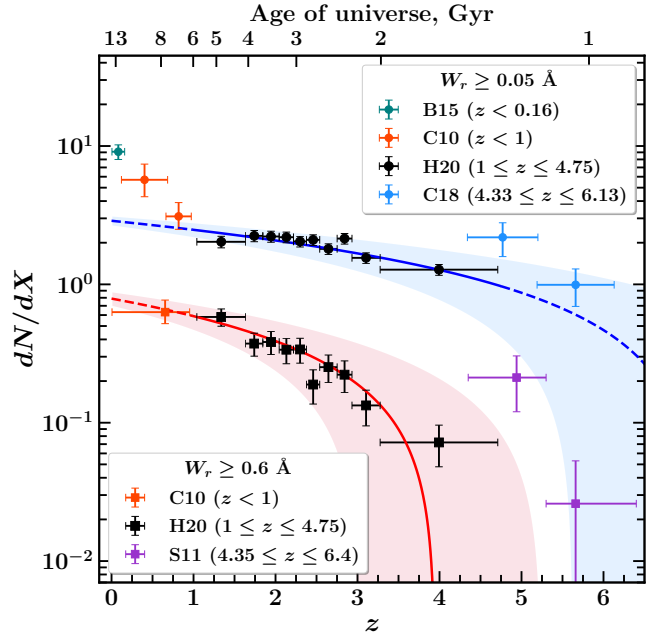


Figure 10. Comparison of our measured dN/dX (black points) over the range $1.0 \leq z \leq 4.75$ with measurements at $z \leq 1$ (Cooksey et al. 2010; Burchett et al. 2015, C10 and B15, respectively) and $z \geq 5$ (Simcoe et al. 2011; Codoreanu et al. 2018, S11 and C18, respectively). Circles represent $W_r \geq 0.05 \text{ \AA}$ and squares represent $W_r \geq 0.6 \text{ \AA}$ absorbers, respectively. Our linear best-fit models (Eq. 15) are overplotted as a solid blue curve for $W_r \geq 0.05 \text{ \AA}$ absorbers and as a solid red curve for $W_r \geq 0.6 \text{ \AA}$ absorbers. Light shadings represent the $\pm 1\sigma$ confidence intervals of the fits. Model extrapolations are shown as dashed curves.

For the weak population, the $W_{r,\text{lim}}$ thresholds for the quoted dN/dX values from Burchett et al. (2015) and Codoreanu et al. (2018) were not precisely equal to 0.05 \AA . We first had to convert their column density thresholds to equivalent width thresholds (there is no uncertainty in the conversion due to thermal broadening because the absorption is on the linear part of the curve of growth). We then applied small correction factors to scale their measured dN/dX to the threshold $W_{r,\text{lim}} = 0.05 \text{ \AA}$.

For the Burchett et al. (2015) data point at $z \simeq 0$, the correction factor was taken as the ratio of the areas under their fitted column density distribution (CDD), which was normalized to dN/dX in the same manner as our EWD (see Eq. 7). The column density corresponding to $W_{r,\text{lim}} = 0.05 \text{ \AA}$ is $\log N = 13.2$ and the correction factor is 1.21. However, Codoreanu et al. (2018) normalized their CDD to the number of completeness-corrected CIV absorbers instead of dN/dX . Therefore, we used the ratio of the areas under our own measured EWD at $2.5 \leq z \leq 4.75$ (for the best-fit parameters shown in Table 3) for both the Codoreanu et al.

(2018) data points at $z > 4.75$. The converted $W_{r,\text{lim}}$ from Codoreanu et al. (2018) at $z \simeq 4.8$ was 0.015 \AA and the correction factor is 0.61; at $z \simeq 5.8$, the converted $W_{r,\text{lim}}$ was 0.06 \AA , and the correction factor is 1.1.

In Figure 10, we present the co-moving path density of CIV for $W_r \geq 0.05 \text{ \AA}$ ($W_{r,\text{lim}} \simeq 0.05 \text{ \AA}$) and for $W_r \geq 0.6 \text{ \AA}$ ($W_{r,\text{lim}} \simeq 0.6 \text{ \AA}$) over the redshift range $0 \leq z \leq 6.4$. Our data ($1.0 \leq z \leq 4.75$) are black points and our model fits and regions of $\pm 1\sigma$ uncertainty are represented by curves and shaded regions, respectively. Absorbers with $W_{r,\text{lim}} \simeq 0.05 \text{ \AA}$ are represented by circles, while those with $W_{r,\text{lim}} \simeq 0.6 \text{ \AA}$ are squares.

4.3.1. The $W_r \geq 0.05 \text{ \AA}$ Population

For the absorber population with $W_r \geq 0.05 \text{ \AA}$ at $z < 1$, the findings of Cooksey et al. (2010) and Burchett et al. (2015) indicate that dN/dX evolves with redshift such that by $z = 0$, the value of dN/dX increases by a factor of roughly 4.5 over our linear model extrapolation. The quantity $n(z)\sigma(z)$ increased by only $\simeq 1.8$ times in 4.5 Gyr (over $1.0 \leq z \leq 4.75$), while in the last ~ 7.7 Gyr ($0 \leq z \leq 1$), it increased by about a factor of $\simeq 4.5$. Interestingly, this is not a dramatic change in terms of cosmic time, as $n(z)\sigma(z)$ increases at a rate of $\sim 0.4 \text{ kpc}^{-1} \text{ Gyr}^{-1}$ (from Eq. 10) at $1.0 \leq z \leq 4.75$ and $\sim 0.6 \text{ kpc}^{-1} \text{ Gyr}^{-1}$ at $z < 1$.

At $z > 4.75$, dN/dX for $W_r \geq 0.05 \text{ \AA}$ measured by Codoreanu et al. (2018) at $5.2 \leq z \leq 6.2$ is consistent within the uncertainties of our model extrapolations. However, there is mild tension between our model and their measured dN/dX for $4.3 \leq z \leq 5.2$. As previously discussed, the correction factor we applied to scale their measured dN/dX was 0.61. If the weak-end slope of the true EWD at $5.2 \leq z \leq 6.2$ is steeper than at $2.5 \leq z \leq 4.75$ (a trend that would be consistent with the redshift evolution we have inferred for the EWD), then the corrected dN/dX value would be in better agreement with the model extrapolation and consistent with a smooth evolution from $z \sim 3$ to $z \sim 6$. For example, to obtain a corrected $dN/dX \simeq 1.0$ to match our model extrapolation, we would require α to evolve from the measured -0.98 at $z \sim 3.5$ to -1.8 at $z \simeq 5$ (yielding a correction factor of 0.29).

Thus, we may infer that linear evolution could remain valid at $z > 4.75$ for $W_{r,\text{lim}} \simeq 0.05 \text{ \AA}$ absorbers if the EWD has a relatively higher frequency of weak absorbers as compared to the average relative frequency over $2.5 \leq z \leq 4.75$ (i.e. with a weak-end slope that is steeper by $\approx 80\%$). Conversely, the data of Codoreanu et al. (2018) may be indicating that CIV-absorbing structures are more common than predicted from a linear extrapolation to $z > 4.75$ and that linear evolution of dN/dX with redshift does not continue to higher redshifts. Either way, additional data (or a reanalysis of the current data to ensure a uniform analysis between studies) would be required to resolve the tension between

the extrapolated linear evolution and the measurement at $4.3 \leq z \leq 5.2$.

4.3.2. The $W_r \geq 0.6 \text{ \AA}$ Population

For the $W_r \geq 0.6 \text{ \AA}$ population at $z < 1$, the reported dN/dX of Cooksey et al. (2010) is consistent with our linear evolution model extrapolated to $z = 0$. This indicates that linear evolution with redshift may be sufficient in describing the incidence of strong systems from $z = 4.75$ to $z = 0$, a cosmic period covering the last $\simeq 12.2$ Gyr of the universe.

For $z > 4.75$, the results are not as clear. The dN/dX values from the survey of Simcoe et al. (2011), as computed and presented by C13, suggest a dramatic rise in strong CIV absorbers between $4.3 \leq z \leq 5.3$ (i.e., for cosmic age ~ 1.0 – 1.6 Gyr) such that dN/dX is a factor of $\simeq 3$ higher at $z \sim 4.3$ than our measured dN/dX . The measured value of dN/dX at $5.3 \leq z \leq 6.3$ (i.e., for cosmic age ~ 0.8 – 1.0 Gyr), is in complete conflict with the extrapolation of our linear evolution model, as the onset redshift for the $W_{r,\text{lim}} = 0.6 \text{ \AA}$ absorber population is roughly $3 \leq z \leq 5.2$ (pink shaded area in Figure 10), suggesting that we should not observe these higher redshift absorbers according to our linear model.

4.3.3. Beyond Linear Evolution?

In summary, there are two concrete conclusions that can be drawn from the $z < 1$ data comprising Figure 10. (1) Evolution of the $W_r \geq 0.05 \text{ \AA}$ absorber population appears to undergo a transition at $z \simeq 1$ such that, the quantity $n(z)\sigma(z)$ increases by a factor of 4–5 from $z = 1$ to $z = 0$ relative to an extrapolation of the linear evolution observed for $1.0 \leq z \leq 4.75$. (2) For $W_r \geq 0.6 \text{ \AA}$, linear evolution appears to hold for $0 \leq z \leq 4.75$, such that the quantity $n(z)\sigma(z)$ increases by a factor of ~ 10 over the last 12.2 Gyr.

Interestingly, linear evolution with redshift does not translate to linear evolution with cosmic time. If the evolution in $n(z)\sigma(z)$ is examined per unit time, the rate is actually a fairly constant ~ 0.4 – $0.6 \text{ kpc}^{-1} \text{ Gyr}^{-1}$ for the $W_r \geq 0.05 \text{ \AA}$ absorber population over the range $0 \leq z \leq 4.75$. The “turn up” in redshift for $z < 1$ is a consequence of a fairly steady evolution and the compression of the time axis with decreasing redshift (see Figure 10). For the $W_r \geq 0.6 \text{ \AA}$ population, the evolution rate is $\sim 1.8 \text{ kpc}^{-1} \text{ Gyr}^{-1}$ for the 4.5 Gyr spanning $1.0 \leq z \leq 4.75$, and $\sim 0.14 \text{ kpc}^{-1} \text{ Gyr}^{-1}$ for the 7.7 Gyr spanning $0 \leq z \leq 1.0$. Thus, from the standpoint of temporal evolution, the strongest systems evolve most rapidly in the early universe and slower in the recent universe, even though their evolution is linear with redshift.

When comparing our dN/dX values with those at $z > 4.75$ for both weak and strong absorber populations, there is unexpected upturn in dN/dX at $z \sim 5$, followed by a decline at $z \sim 6$. Our measured dN/dX (and that of C13 from their SDSS survey) shows a smooth and

steadily decrease with increasing redshift as $z = 5$ is approached, and this trend might be expected to continue to higher redshifts. Thus, the elevated dN/dX at $z \sim 5$ for both weak and strong absorbing structures from the infrared surveys of [Simcoe et al. \(2011\)](#) and [Codoreanu et al. \(2018\)](#) places some tension on our expectations of CIV evolution between the first and second billion years of the universe.

Notably, the [Simcoe et al. \(2011\)](#) measurement at $4.3 \leq z \leq 5.3$ for $W_{r,\text{lim}} = 0.6 \text{ \AA}$ is based on only two CIV absorbers and the $5.3 \leq z \leq 6.3$ measurement is based on just one absorber. Furthermore, the values reported by [Codoreanu et al. \(2018\)](#) for $W_{r,\text{lim}} \simeq 0.05 \text{ \AA}$ incorporated 30 CIV absorbers for the $4.3 \leq z \leq 5.2$ measurement and six for the $5.2 \leq z \leq 6.2$ measurement. However, these 36 absorbers were found in only four quasar spectra. As such, it is not implausible that there may exist some systematic uncertainties, such as cosmic variance, in these high-redshift infrared surveys.

On the other hand, the redshift path coverage of optical surveys declines at $z > 3$ (see [Figure 3](#)), so that in order to reduce the uncertainties in dN/dX , the redshift bin is extended. This has the effect of averaging across a larger redshift range and the loss of “redshift resolution” for $z \simeq 3$ to $z \simeq 4.75$. This may be blurring our ability to resolve an upward trend in our data in this redshift range.

Alternatively, the infrared data may reflect a true rise in the cosmic incidence of CIV absorbers in a short period of time, only to fall again in a few hundred million years. Though a physical argument for such behavior may be difficult to formulate and may appear to be contrived at face value, it cannot yet be ruled out. For example, such a scenario might require chemical enrichment in both high and low overdensity astrophysical environments in such a manner that the different ionization conditions in these different environments constrain both optically thin and optically thick absorbing structures to evolve similarly over the same narrow cosmic time period. Future observational programs to study the high-resolution spectra of a large number of high-redshift quasars would be key for resolving the tension in the measured CIV absorber evolution.

4.4. Sizes of CIV Absorbing Structures

To gain further insight into the statistical cross section of CIV absorbers, we estimate the $\sigma(z)$ of the gas complexes associated with different populations of CIV absorbers from $N_x(z) = (c/H_0)n(z)\sigma(z)$ ([Eq. 10](#)). For this exercise, we assume that these complexes are the gaseous halos of galaxies, or the CGM. We adopt the standard [Holmberg \(1975\)](#) scaling relation between galaxy luminosity, L , and halo absorbing gas radius, $R(L) = R_*(L/L_*)^\beta$, where $\beta \approx 0.3\text{--}0.4$ (e.g., [Chen et al. 2001](#); [Kacprzak et al. 2008](#); [Nielsen et al. 2013](#)), and R_* is the effective absorbing gas halo radius for an L_* galaxy. For a given luminosity, the gaseous halo cross

section is $\sigma(z) = \pi f_c(z)R^2(L)$, where $f_c(z)$ is the covering fraction of the absorbing gas, which may change with redshift (see e.g. [Nielsen et al. 2013](#)).

The cosmic number density of gas structures, $n(z)$, is given by the observed number density of galaxies, obtained by integrating the galaxy luminosity function. We adopt the fitted Schechter functions of [Parsa et al. \(2016\)](#), who provide the functional parameters $\alpha(z)$, $L_*(z)$, and $\phi_*(z)$ as fitted functions of redshift for $0 \leq z \leq 8$. We then integrated the product $n(z)\sigma(z)$ over luminosity from a minimum luminosity of $L_{\text{min}}(z) = 0.1L_*(z)$ to infinity, and obtain

$$R_*(z) = \left[\frac{H_0}{\pi c f_c(z) \phi_*(z)} \frac{N_x(z)}{\Gamma[x(z), l(z)]} \right]^{1/2}, \quad (17)$$

where $\Gamma(a, b)$ is the upper incomplete Gamma function ([Abramowitz & Stegun 1972](#)), $N_x(z)$ is the measured dN/dX at redshift z , $l(z) = L_{\text{min}}(z)/L_*(z) = 0.1$, and $x(z) = 2\beta + \alpha(z) + 1$. We assume $\beta = 0.35$.

In [Table 7](#), we present selected rounded values of R_* for three redshifts in the range $1.0 \leq z \leq 4.75$ for three populations, $W_{r,\text{lim}} = 0.05, 0.3, \text{ and } 0.6 \text{ \AA}$. We assume a unity covering fraction, where $R_* \propto f_c(z)^{-1/2}$. For $W_r \geq 0.05 \text{ \AA}$ absorbers, R_* ranges from $\sim 210 \text{ kpc}$ at $z \simeq 4$ to $\sim 240 \text{ kpc}$ at $z \simeq 2.5$, which holds roughly constant down to $z \simeq 1.3$. For $W_r \geq 0.3 \text{ \AA}$ absorbers, we obtained $\sim 90 \text{ kpc}$ at $z \simeq 4$ to $\sim 150 \text{ kpc}$ at $z \simeq 1.3$. And for $W_r \geq 0.6 \text{ \AA}$ absorbers, R_* ranges from $\sim 50 \text{ kpc}$ at $z \simeq 4$ to $\sim 120 \text{ kpc}$ at $z \simeq 1.3$. The typical uncertainties on R_* from propagating errors on $N_x(z)$ are on the order of $\sim 10\text{--}20\%$.

Table 7. Characteristic Absorbing Halo Sizes for an L_* Galaxy

$W_{r,\text{lim}}$ (\AA)	$R_*(z \simeq 1.3)$ (kpc)	$R_*(z \simeq 2.5)$ (kpc)	$R_*(z \simeq 4.0)$ (kpc)
0.05	230	240	210
0.3	150	130	90
0.6	120	80	50

Under the assumption that $n(z)$ of CIV absorbers is given by the galaxy luminosity function, the exercise indicates that R_* for $W_r \geq 0.05 \text{ \AA}$ absorber structures grows at a rate of $\sim 30 \text{ kpc}$ in $\approx 1.5 \text{ Gyr}$ (from $z = 4$ to $z = 2.5$) and then remains constant (within the uncertainties) until $z \sim 1$. For the $W_r \geq 0.3 \text{ \AA}$ absorbers, R_* increases steadily and monotonically by $\approx 13 \text{ kpc Gyr}^{-1}$ for the 4.5 Gyr period covered by our survey, while the rate of increase of the $W_r \geq 0.6 \text{ \AA}$ absorbers is $\approx 16 \text{ kpc Gyr}^{-1}$. These estimates can be considered lower limits, as R_* increases as the inverse square root of the covering fraction.

We did not take into account the possibility of different absorber populations being primarily associated with different types of galaxies; e.g. stronger absorbers associated with brighter galaxies. For example, C13 estimated R_* for $W_r \geq 0.6 \text{ \AA}$ absorbers assuming these absorbers reside only in the halos of galaxies brighter than $L_{min} = 0.5L_*$. They obtained $R_* \approx 50 \text{ kpc}$ at $1.46 \leq z \leq 4.55$ (noting $\sim 20 - 60\%$ uncertainties in their calculated galaxy number densities). If we adopt $L_{min} = 0.5L_*$, our estimated R_* increases by $\sim 50\%$ at $z \simeq 1.3$, yielding $\sim 180 \text{ kpc}$, and by $\sim 60\%$ at $z \simeq 4$, yielding $\sim 80 \text{ kpc}$. Any differences between our estimate and that of C13 are likely due to the adoption of different luminosity functions and L_{min} .

There is a well-established anti-correlation between the strength of CIV absorption and impact parameter from the host galaxy (Chen et al. 2001; Chen 2012; Liang & Chen 2014; Bordoloi et al. 2014), which is interpreted as the absorption strength decreasing with galactocentric distance. At $z \sim 2.5$, Adelberger et al. (2005) and Steidel et al. (2010) found CIV absorption out to $\sim 100 \text{ kpc}$ around Lyman Break Galaxies, with the strength of absorption decreasing with increasing impact parameter. Adelberger et al. (2005) notes that a $W_r = 0.6 \text{ \AA}$ CIV absorber would have a typical impact parameter of 80–85 kpc. Our estimates of R_* for the absorber populations defined by $W_r \geq 0.3 \text{ \AA}$ and $W_r \geq 0.6 \text{ \AA}$ are in good agreement with these findings.

The virial radius of a Milky Way-sized galaxy halo is $\approx 200 \text{ kpc}$ at $z = 0$ (Navarro et al. 2010). Given our estimates for R_* of 210 to 240 kpc from $z \simeq 4$ to $z \simeq 1.3$, and since the virial radius of Milky Way-like galaxies is substantially smaller at higher redshift, we may infer that some fraction of the weakest absorbers reside outside the virial radius of galaxies and perhaps even in the IGM. This may also hold true at $z \simeq 0$, where we estimate $R_* \approx 450 \text{ kpc}$ for $W_r \geq 0.05 \text{ \AA}$ based on the data of Burchett et al. (2015). An understanding of how metals escape hundreds of kiloparsecs from the galaxies wherein they are produced will likely be developed through detailed theoretical modeling with physically accurate feedback prescriptions.

4.5. Physical Interpretations

As discussed above, the statistical evolution of CIV absorbers can be understood in terms of the evolution of the product $n(z)\sigma(z)$. Physically, these quantities evolve due to changes in the column densities of the absorbing clouds and the kinematic and dynamical motions of absorbing gas structures. The monotonic increase in the evolution constant A with increasing $W_{r,lim}$ suggests that the evolution of absorbing clouds is more rapid for more optically thick and/or kinematically complex absorbers. That is, the rate of increase of the product $n(z)\sigma(z)$ with time is higher for these absorbers than for optically thin and/or kinematically simple absorbers (which dominate the overall CIV absorber population).

There are two factors that govern the evolution of CIV absorbers. The first is the metal enrichment history of the IGM and CGM and the second is the nature of the ionization of carbon, which is dependent on both the intensity and spectral energy distribution of the ionizing spectrum local to the absorbing structures and the optical depth of the absorbing structures themselves. We first consider the chemical enrichment history and then the nature of the ionization physics.

Schaye et al. (2003) used pixel statistics obtained from UVES and HIRES data to derive a model of the metallicity distribution ($[C/H]$) in the IGM and concluded that there was little enrichment across $2 \leq z \leq 4$, implying that most of the enrichment must have taken place prior to $z \sim 4$. Indeed, the CIV mass density, Ω_{CIV} , is observed to be effectively unchanging across $1.5 \leq z \leq 4.5$ (Pettini et al. 2003; Songaila 2005; Scannapieco et al. 2006; Boksenberg & Sargent 2015). Cooke et al. (2010) combined their Ω_{CIV} measurements at $z < 1$ with those at higher redshift and found only a shallow rise in Ω_{CIV} from $z \sim 5$ to the present epoch.

Unfortunately, Ω_{CIV} is not an ideal tracer of the total carbon mass density, Ω_C , because $\Omega_{CIV} \ll \Omega_C$ (Schaye et al. 2003). Furthermore, Ω_{CIV} is dominated by the few highest column density CIV absorbers and is thus sensitive to the range of column densities observed, which can be dependent on the total redshift path covered in a survey. Incorporating ionization corrections, Simcoe (2011) found that Ω_C increased a factor of no more than two from $z \sim 4.3$ to $z \sim 2.4$, which they showed is consistent with the estimated amount of carbon ejected into the CGM and IGM via supernovae feedback.

Given that the cosmic star formation rate density peaked around $z \sim 2$ (e.g., Madau & Dickinson 2014), it would seem reasonable that metal enrichment of the IGM and CGM occurred at redshifts much lower than $z \simeq 4$. Indeed, the period known as “cosmic noon”, defined as the epoch at which galaxies assembled roughly half of their stellar mass, occurred at $1.5 \leq z \leq 3$ (e.g., Murphy et al. 2011; Behroozi et al. 2013; Feldmann et al. 2016). This epoch also saw the peak in galactic-scale outflows from stellar processes (e.g., Rupke 2018). Large observational programs are currently underway to characterize the CGM, including CIV absorbers, at cosmic noon (e.g. Nielsen et al. 2020). The measured dN/dX of CIV absorbers exhibits only a slow, steady increase during cosmic noon, which at face value, does not suggest a substantial rise in the carbon abundance in the CGM and IGM in this period. The slow rise in dN/dX is, however, consistent with a steady increase in the mean metallicity of the universe from $z \sim 5$ to $z \sim 0$ (e.g., Rafelski et al. 2012; Lehner et al. 2016; McQuinn 2016; De Cia et al. 2018).

For $1.0 \leq z \leq 4.75$, it is an open question as to what degree the evolution of the metagalactic ionizing background, both globally and local to CIV-absorbing structures, drives the observed evolution of dN/dX . Of par-

ticular interest in this regard is to pose the question of how the UVB may govern the linear evolution of $n(z)\sigma(z)$ with redshift such that the rate of evolution increases for progressively larger $W_{r,\text{lim}}$ populations (recall that we find $A \propto W_{r,\text{lim}}$, see Table 6). According to linear evolution, for a given $W_{r,\text{lim}}$, the evolution of $n(z)$ and $\sigma(z)$ are constrained by Eq. 16.

The average global UVB has been known to become harder (increased relative proportion of higher energy photons) with time (e.g., Faucher-Giguère et al. 2009; Haardt & Madau 2012; Puchwein et al. 2019), allowing the CIV transition to dominate over lower-ionization transitions. Theoretical models have often assumed the UVB is spatially homogeneous and externally imposed (e.g., Oppenheimer et al. 2010; van de Voort et al. 2011; Keating et al. 2016; Rahmati et al. 2016), but such models have often been unsuccessful in reproducing observed properties of CIV absorbers at $z \geq 4$ (Oppenheimer et al. 2009; Rahmati et al. 2016; Finlator et al. 2016; Finlator et al. 2018). High redshift observational studies have also identified a need for variations in the local ionizing radiation field around absorbers (e.g., D’Odorico et al. 2013; Boksenberg & Sargent 2015; Morrison et al. 2019).

While the reionization of hydrogen produces inhomogeneities in the UVB only at $z > 5$, helium reionization creates significant spatial variations that persist to $z \simeq 3$ (e.g., Becker et al. 2011). This is due to the shorter mean free path of HeII-ionizing photons and the high ionization potential of HeII (4 Ryd) which requires highly energetic sources with “hard” spectra, such as quasars (Faucher-Giguère et al. 2008). By the end of HeII reionization near $z \simeq 3$, isolated regions as large as ~ 50 Mpc, characterized as “HeIII bubbles”, can have a harder UVB spectral energy distribution relative to the average UVB spectral distribution (McQuinn et al. 2009; Furlanetto 2009).

Since the C^{+3} and He^+ ions have very similar ground-state ionization energies, the fraction of carbon in the C^{+3} ionization stage will vary in relation to the HeII ionization edge opacity, which governs the hardness of the local UVB for energies above 4 Ryd. Worseck et al. (2016) show that these HeIII bubbles persist for over ~ 600 Myr past the end of HeII reionization, lasting until at least $z \sim 2.7$. These HeIII bubbles therefore persist into the early period of cosmic noon, when galaxies begin to contribute HI and HeII ionizing photons to the UVB (e.g., Haardt & Madau 2012). As cosmic noon is dialing down by $z = 1.5$, we see that the behavior of the UVB and its influence on the ionization balance of carbon, and thus the incidence of CIV absorbers, is dramatically evolving in both its homogeneity and spectral energy distribution over the redshift range $1.0 \leq z \leq 4.75$.

Given the complexity of the evolution of the UVB, it is remarkable that dN/dX of CIV absorbers shows a monotonic linear increase with decreasing redshift over the 4.5 Gyr cosmic time covered by our survey. Interestingly, Simcoe (2011) found that CIV and higher-

ionization species are more abundant relative to CIII and lower ionization species from $z = 4.3$ to $z = 2.4$; a result that generally supports a trend in which higher ionization states are favored at later times (see also Becker et al. 2019). This is consistent with a rise in the incidence of CIV absorbers with cosmic time.

Our results for the onset redshift z_0 suggest that the population dominated by weak absorbers, i.e., $W_{r,\text{lim}} = 0.05 \text{ \AA}$, would be present as soon as $z \sim 8$ (when the universe was ~ 600 Myr old), whereas absorbers with $W_{r,\text{lim}} = 0.6 \text{ \AA}$ would appear no earlier than $z \sim 4$ (when the universe was about 1.8 Gyr old). This would imply that optically thin CIV clouds came into existence in the midst of the epoch of HI reionization (e.g., Gnedin & Ostriker 1997; Gnedin 2000; Barkana & Loeb 2001), whereas optically thick and/or kinematically complex clouds arose following the completion of this epoch (e.g., Bolton & Haehnelt 2007; Robertson et al. 2013). Establishing the redshifts at which CIV absorbers first arise would provide insights into the origins of cosmic carbon enrichment, the early mechanisms by which metals are distributed into the IGM and CGM, and details into the transmission and spectral shape of the ionizing radiation field during the epoch of HI reionization (e.g., Becker et al. 2015; Finlator et al. 2015).

Whether the origins and physical processes affecting the weakest absorbers is distinct from that of the strongest absorbers is an open question. Though some studies find evidence to relate CIV to galactic winds (e.g., Fox et al. 2007; Steidel et al. 2010), strong MgII is likely a better tracer of such outflows as their evolution mimics the star formation and stellar-driven outflow activity of the universe (e.g., Ménard et al. 2011; Matejek & Simcoe 2012; Zhu & Ménard 2013; Chen et al. 2015). Songaila (2006) points out that very weak CIV absorbers would require unreasonably large outflow velocities if they were associated with galactic outflows. Alternatively, they argue that these weak absorbers could be ionized by active galactic nuclei (AGN) spectra, rather than by local galaxies or the global UVB.

However, if local AGN were indeed the primary culprits behind the incidence of weak CIV absorbers, then we would expect dN/dX for $W_r \geq 0.05 \text{ \AA}$ to trace the AGN activity of the universe. As shown in Figure 10, dN/dX for weak absorbers does not peak around $z \sim 2$ nor does it decline at later times that would mirror the observed AGN luminosity function or cosmic black hole accretion rate (e.g., Shankar et al. 2009; Kulkarni et al. 2019; Shen et al. 2020). On the contrary, dN/dX for weak absorbers rises rapidly with decreasing redshift only below $z = 1$, well after the epoch of peak AGN activity. This is also further evidence against outflows being the source of weak CIV since star formation activity peaks around $z \sim 2$. At the very least, we would expect a relatively more rapid increase in CIV dN/dX from higher redshifts to $z \sim 2$ if outflows were the source of CIV.

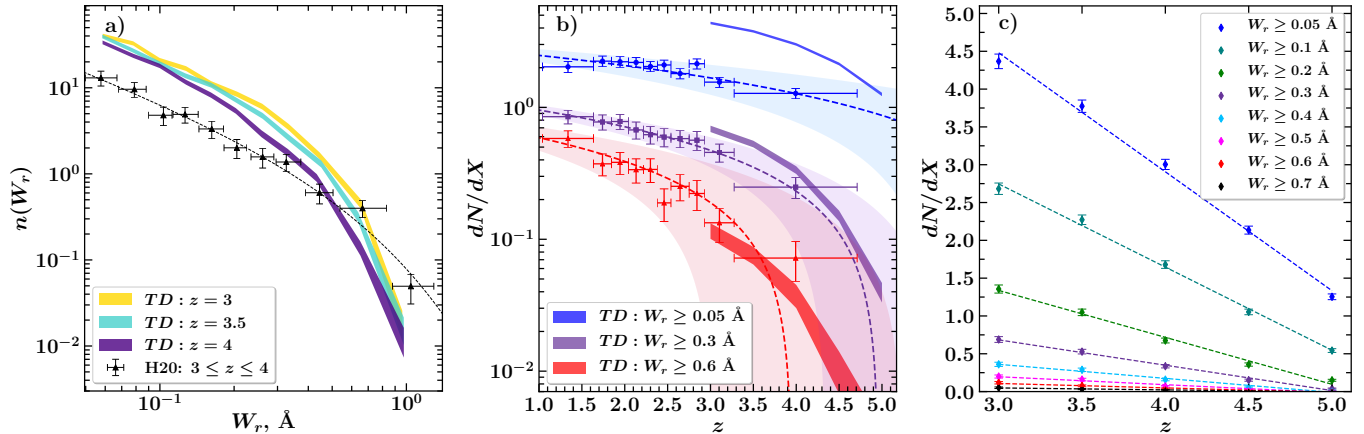


Figure 11. (a) Our observed EWD data points, with best-fit Schechter function parameterization represented by a dashed black curve, at $3 \leq z \leq 4$, compared to the TD simulations at $z = 3$, $z = 3.5$, and $z = 4$ (represented by colored shading). (b) Our observed dN/dX (data points and error bars), compared to the TD simulations at $z = 3$ (opaque bands). Our linear best-fit evolution models (Eq. 15) are overplotted in blue, purple, and red dashed lines for $W_r \geq 0.05 \text{ \AA}$, $W_r \geq 0.3 \text{ \AA}$, and $W_r \geq 0.6 \text{ \AA}$ absorbers, respectively, with light shading depicting the $\pm 1\sigma$ confidence intervals for those fits. (c) dN/dX as a function of redshift, for different $W_{r,\text{lim}}$ in the TD simulations. The dashed lines show the linear best-fit models for each absorber species.

4.6. Theoretical Explorations

To augment our theoretical understanding of the observed characteristics and evolution of CIV at high redshift, we compared our observations to the predictions of the cosmological radiation hydrodynamic simulations TECHNICOLOR DAWN (TD, Finlator et al. 2018). The TD simulations model galaxy growth and the baryon cycle, while self-consistently modeling an evolving multi-frequency, spatially-inhomogeneous UVB. Though the TD simulations accurately reproduce observations of the galaxy stellar mass function, the co-moving path density of CII and SiIV absorbers, and the mean transmission in the Ly α forest, at $z \geq 5$ they underproduce the dN/dX of strong CIV absorbers (Finlator et al. 2018; Doughty & Finlator 2019; Finlator et al. 2020). Similar results have been reported for the EAGLE simulations (Rahmati et al. 2016).

Though Finlator et al. (2020) showed that this underabundance of CIV absorbers could be evidence for density-bounded ionizing escape, this interpretation is not unique in that it is degenerate with the possibility that the intrinsic stellar emission is too “soft” (deficient in CIV ionizing photons; see Zackrisson et al. 2013). Either way, the cosmic epoch of $z \geq 5$ is complicated to simulate as it covers the immediate aftermath of HI reionization and the earliest stages of HeII reionization. Previous comparisons of CIV observations to the TD simulations have been restricted to $z \gtrsim 5$ and focused on column densities (Finlator et al. 2018, 2020). Here, with our improved observational constraints on the EWD and dN/dX of CIV for $z < 5$, we investigate whether the TD simulations reproduce observed CIV statistics at the slightly lower redshift range $z = 3$ to $z = 5$, under the assumption of ionization-bounded escape.

We generated a sample of CIV absorbers from the TD simulations at $z = 3.0, 3.5, 4.0, 4.5$, and 5.0 . The TD spectra and CIV absorption lines were generated as described in Finlator et al. (2018) using instrumental parameters (resolution, pixel sizes, and pixels per resolution element) consistent with the HIRES and UVES spectrographs. The signal-to-noise ratio of the spectra was fixed at 50 per pixel, which ensures that the TD spectra are 100% complete to a 5σ detection threshold of $W_r = 0.05 \text{ \AA}$. To ensure that both the absorber incidence and EWDs are consistent with our survey, we define a single absorber in the TD spectra to include all absorption components within a $\pm 500 \text{ km s}^{-1}$ window (see Section 2.3). The TD simulated CIV absorber catalogs contain a total of $\sim 10,000$ absorbers with $W_r \geq 0.05 \text{ \AA}$.

In Figure 11(a), we compare our observed EWD at $3 \leq z \leq 4$ to the EWDs from TD at $z = 3.0, 3.5$, and 4.0 . We limited the comparison for the EWD to this redshift range because (1) we have robust statistics in this range of our survey, and (2) we aim to examine a regime cleanly segregated from $z \geq 5$. The TD EWD was computed from the simulated CIV absorber catalog using methods identical to those we applied to our observational data (see Section 3.1).

Comparison with our observations indicates that TD is most successful at reproducing the frequency of CIV absorbers in the equivalent width range $0.4 \leq W_r \leq 0.8 \text{ \AA}$. At the strong end, simulations underproduce absorbers with $W_r \sim 1 \text{ \AA}$ by roughly a factor of five. Moreover, they entirely fail to produce stronger absorbers with $W_r > 1.1 \text{ \AA}$. These discrepancies echo previous indications that cosmological simulations underproduce strong CIV absorbers (Finlator et al. 2020) or, equivalently, Ω_{CIV} at $z > 4$ (Rahmati et al. 2016).

Our unprecedented dynamic range in W_r now reveals that the problem is not a simple offset in normalization. TD *over*produces weak absorbers with $W_r \leq 0.4 \text{ \AA}$ by a factor that increases from ~ 2 for $W_r \leq 0.3 \text{ \AA}$ to ~ 3 for $W_r \leq 0.15 \text{ \AA}$. The higher frequency of $W_r \leq 0.3 \text{ \AA}$ absorbers in TD relative to observations suggests that the solution to the CIV mismatch may not be as simple as uniformly boosting the overall carbon yield or hardening the UVB.

In Figure 11(b), we compare the $3 \leq z \leq 5$ observed co-moving path densities, dN/dX , with the TD dN/dX predictions. The data points show the observational measurements for $W_r \geq 0.05 \text{ \AA}$, $W_r \geq 0.3 \text{ \AA}$, and $W_r \geq 0.6 \text{ \AA}$. The dashed and shaded regions show our best-fit linear evolution models and uncertainties (see Section 3.3). The opaque bands show the predicted dN/dX from the TD CIV absorber catalog, where the thickness reflects Poisson uncertainties. These values and their uncertainties were computed using identical methods to those we applied to the observational data (see Section 3.2).

At $3 \leq z \leq 5$, the behavior of dN/dX as predicted by TD is more or less consistent with the uncertainties in the data for $W_r \geq 0.3 \text{ \AA}$ and $W_r \geq 0.6 \text{ \AA}$ absorbers, though there is an over-abundance of $W_r \geq 0.3 \text{ \AA}$ absorbers at $z = 3$. On the other hand, TD overpredicts dN/dX of $W_r \geq 0.05 \text{ \AA}$ absorbers across the full range of $z = 3\text{--}5$ with the discrepancy increasing up to a factor of roughly three by $z = 3$. Interestingly, the redshift evolution of the TD CIV absorbers is such that dN/dX for a given $W_{r,\text{lim}}$ declines toward higher redshifts in a qualitatively similar manner as the observations. To quantify this behavior, we examined whether a model of linear decrease in dN/dX with increasing redshift describes the evolution in the simulated catalogs, as it did our observations in Section 3.3.

In Figure 11(c), we show that the dN/dX of different species of absorbers defined by progressively increasing $W_{r,\text{lim}}$ all decrease linearly with increasing redshift, with the rate of this evolution (represented by the slope of each best-fit line) increasing towards lower $W_{r,\text{lim}}$. Though the linear fits to the simulated data were performed over a smaller redshift range than the observed data, they agree with the qualitative outcomes that (1) the co-moving path density of CIV absorbers increases with cosmic time, and (2) the evolution is progressively more rapid as the optical depth and/or kinematic complexity of the CIV gas clouds increase.

The degree of agreement between the TD predictions and the observed CIV absorber statistics at $z = 3$ to $z = 5$ is encouraging, and leads us to consider various aspects of the physical modelling that do and do not yield agreement with the observations. One possibility for why the simulated abundances better match the observations at $z < 5$ is that a reduction in spatial fluctuations in the simulated UVB as the epoch of HI reionization reaches completion and as HeII reionization advances, may re-

sult in higher incidences of CIV absorbers. Furthermore, as mentioned above, the observed mean intensity of the UVB increases with decreasing redshift.

However, it is difficult to understand the predicted over-abundance of the weaker CIV absorbers, because TD yields a UVB mean intensity at $z < 5$ that is weaker than what is observed (Hassan et al. 2020). A higher mean intensity would improve TD’s slight discrepancy with the observed mean transmission in the Ly α forest (Finlator et al. 2018), but would further increase the incidence of weak CIV. Alternatively, the overprediction of weak CIV by TD may indicate problems with the feedback model in that the simulated outflows could eject too many metals or expel them too far from galaxies. If outflows eject metals too far from galaxies, then we might expect too little power in the velocity clustering function of weak CIV absorbers in TD (see Finlator et al. 2018, 2020). If outflows remove too much (or not enough) gas from low-mass galaxies, then we would expect the UV luminosity function and/or stellar mass function to depart from observations at the faint end.

Finally, because the simulations are quite successful at reproducing the observed linear redshift-evolution of CIV absorbers from $z = 5$ to $z = 3$, the TD predictions place further tension on the apparent observed “bump” in the dN/dX at $z \sim 5$ (Simcoe et al. 2011; Codoreanu et al. 2018, see Figure 10). A theoretical physical mechanism for such cosmically brief enhancement is difficult to understand.

5. CONCLUSION

We conducted a survey of archival high-resolution Keck/HIRES and VLT/UVES spectra ($\sim 6.6 \text{ km s}^{-1}$) of 369 quasars spanning the range of emission redshifts $1.1 \leq z_{\text{em}} \leq 5.3$. The high survey sensitivity allowed us to characterize, for the first time, the distribution and evolution of the weakest CIV absorption systems with $W_r < 0.3 \text{ \AA}$, as well as stronger absorbers with $W_r \geq 0.3 \text{ \AA}$. Using automated CIV doublet detection, combined with visual inspections to verify each candidate CIV absorber, we measured the equivalent widths of the absorbers and quantified the detection thresholds, redshift path lengths, and completeness limits of our survey. We find that we are $\sim 50\%$ complete at $W_r = 0.05 \text{ \AA}$, and limit our scientific analysis to absorbers with equivalent widths above this threshold; our survey is $\sim 100\%$ complete to absorbers with $W_r \geq 0.3 \text{ \AA}$.

Over a total co-moving redshift path of $\Delta X \simeq 803$, we detected 1318 CIV absorbers with $W_r \geq 0.05 \text{ \AA}$, within the redshift range $1.0 \leq z \leq 4.75$. This corresponds to a cosmic age from $\sim 1.5 \text{ Gyr}$ ($z = 4.75$) to $\sim 6 \text{ Gyr}$ ($z = 1.0$), a roughly $\sim 4.5 \text{ Gyr}$ period from when the universe was $\sim 10\%$ to $\sim 45\%$ of its present age. Using data from the literature, we extended our study to cover the redshift range $0 \leq z \leq 6.4$. We then compared our observational results to theoretical predictions from

hydrodynamic cosmological simulations.

1. The EWD of CIV is well-fit by a Schechter function (see Figure 5), with a power law slope of $\alpha \simeq -0.9$ and a characteristic equivalent width of $W_\star \simeq 0.5 \text{ \AA}$. In the range $1.0 \leq z \leq 4.75$, the EWD evolves from $z < 2.5$ to $z \geq 2.5$ such that the power-law slope increases by $\sim 20\%$ and the normalization decreases by $\sim 20\%$. This suggests that the cosmic incidence of weaker CIV absorbers relative to stronger CIV absorbers increases toward higher redshift.
2. The co-moving redshift path density, dN/dX , increases with cosmic time (decreases with redshift), with the rate of the increase being larger as the population is limited to progressively higher W_r absorbers (see Figure 6). From $z = 4.75$ to $z = 1$, dN/dX rises by a factor of ~ 1.8 for $W_r \geq 0.05 \text{ \AA}$ absorbers, ~ 3.3 for $W_r \geq 0.3 \text{ \AA}$ absorbers, and ~ 8.1 for $W_r \geq 0.6 \text{ \AA}$ absorbers.
3. The evolution of dN/dX is well-described by a linear model. We successfully parameterize the linear evolution as a function of the minimum W_r of a population, $W_{r,\text{lim}}$, using three parameters (see Section 3.3), $\langle N_x \rangle$, the cosmic mean of dN/dX , A , the evolution constant, and f_0 , the extrapolated value of dN/dX at $z = 0$. An additional parameter is z_0 , the onset redshift. The model fits yield a quantitative picture of linear CIV absorption in which populations with progressively higher $W_{r,\text{lim}}$ evolve faster and have smaller cosmic mean incidence. Simple extrapolation of the model yields the expectation that populations with progressively higher $W_{r,\text{lim}}$ might make their first appearance in the universe at later times than populations defined by lower $W_{r,\text{lim}}$.
4. For absorbers with $W_r \geq 0.05 \text{ \AA}$ and absorbers with $W_r \geq 0.6 \text{ \AA}$, we extended our dN/dX measurements for $1.0 \leq z \leq 4.75$ with those from the literature for $z < 1$ and for $z > 4.75$, thus examining CIV evolution across $0 \leq z \leq 6.4$ (see Figure 10). For $z \leq 1$, the evolution remains consistent with our linear model for $W_r \geq 0.6 \text{ \AA}$ absorbers. However, for $W_r \geq 0.05 \text{ \AA}$ absorbers, the evolution rapidly increases relative to the linear extrapolation. For $z > 4.75$, both populations of absorbers have higher dN/dX than what would be expected based on extrapolation of linear evolution. It is not clear if this is due to small number statistics in the high redshift measurements, or if there is an increase in CIV absorbing structure over a brief $\simeq 0.5 \text{ Gyr}$ period around $z \simeq 5$. We argue that it is difficult to understand such rapid evolution at that epoch.
5. Assuming the gas structures hosting CIV absorbers are the halos of galaxies, we estimate

the CIV absorbing halo radius, R_\star , for an L_\star galaxy. For $W_r \geq 0.05 \text{ \AA}$ absorbers, R_\star grows from $\sim 210 \text{ kpc}$ at $z \simeq 4$ to $\sim 240 \text{ kpc}$ at $z \simeq 2.5$, becoming relatively constant until $z \simeq 1$. For $W_r \geq 0.6 \text{ \AA}$ absorbers, R_\star grows from $\sim 50 \text{ kpc}$ at $z \simeq 4$ to $\sim 120 \text{ kpc}$ at $z \simeq 1.3$. The large halo sizes for the weakest absorbers would suggest that they could be found in the outer extremes of the CGM and that some fraction may even reside in the IGM.

6. A $3 \leq z \leq 5$ mock survey of CIV absorbers using the TECHNICALOR DAWN simulations of Finlator et al. (2018) indicates that the simulations match the observed EWD and dN/dX of CIV absorbers more accurately in this redshift range than they do at $z > 5$ (see Finlator et al. 2020). Furthermore, consistent with our linear evolution model, the simulations yield CIV absorber populations for which dN/dX decreases linearly with increasing redshift and for which the rate of evolution increases as $W_{r,\text{lim}}$ is increased. The major discrepancy between our observations and the simulations at $z < 5$ is the over-abundance of weak absorbers with $W_r \leq 0.3 \text{ \AA}$, implying the need for modifications to the simulated UVB and/or the feedback model.

We discussed the observed CIV evolution in terms of a changing metal content and a changing metagalactic UV background of the universe. Whatever the details of the physical mechanisms manifesting the observed evolution may be, we can still infer that the rise in cosmic incidence of all populations of CIV absorbers implies that the structures they trace become increasingly more common with cosmic time due to higher cosmic number density and/or larger physical size (physical cross section).

Our estimates of the sizes of the gas structures that comprise CIV absorbers would suggest that, though the very strongest CIV absorbers reside well within the virial radii of galaxies, CIV absorbing gas clouds with $W_r \leq 0.3 \text{ \AA}$ likely persist out to the extreme limits of the CGM and may bridge the interface with the IGM. The weakest absorbing clouds could possibly even reside in the IGM, perhaps residing in the gaseous filamentary structures that interconnect galaxies. We wish to explore this in future work, as well as explore the evolution in the kinematics of CIV.

ACKNOWLEDGMENTS

We thank Kathy Cooksey, Valentina D’Odorico, Jane Charlton, and Joe Burchett for helpful discussions regarding this work. C.W.C. thanks the National Science Foundation for the grants AST-0708210 and AST-1517816, which partially supported this work. N.M.N., G.G.K., and M.T.M. acknowledge the support of the Australian Research Council through *Discovery Project* grant DP170103470. M.T.M. also thanks the Australian Research Council for *Discovery Project* grant DP130100568 for their partial support of this work. Parts of this research were supported by the Australian Research Council Centre of Excellence for All Sky Astrophysics in 3 Dimensions (ASTRO 3D), through project number CE170100012.

We dedicate this paper to the memory of Dr. Wallace Leslie William Sargent, who was a pioneer of the field of quasar absorption lines and so positively influenced the lives and careers of multiple generations of astronomers. This research has made use of the services

of the ESO Science Archive Facility. Some of the data presented herein were obtained at the W. M. Keck Observatory, which is operated as a scientific partnership among the California Institute of Technology, the University of California, and the National Aeronautics and Space Administration and made possible by support of the W. M. Keck Foundation. The authors wish to recognize and acknowledge the very significant cultural role and reverence that the summit of Maunakea has always had within the indigenous Hawaiian community. We are most fortunate to have the opportunity to conduct observations from this mountain.

Facilities: VLT: Kueyen (UVES), Keck: I (HIRES).

Software: ASTROPY (Astropy Collaboration et al. 2013), MATPLOTLIB (Hunter 2007), NUMPY (Oliphant 2006), SCIPY (Virtanen et al. 2020), IPYTHON (Perez & Granger 2007), SYSANAL (Churchill 1997), SEARCH (Churchill et al. 1999), IRAF (Tody 1986), UVES_POPLER (Murphy et al. 2016), MAKEE (Barlow 2005).

REFERENCES

- Abramowitz, M., & Stegun, I. A. 1972, Handbook of Mathematical Functions
- Adelberger, K. L., Shapley, A. E., Steidel, C. C., et al. 2005, *ApJ*, **629**, 636
- Anglés-Alcázar, D., Faucher-Giguère, C.-A., Kereš, D., et al. 2017, *MNRAS*, **470**, 4698
- Astropy Collaboration, Robitaille, T. P., Tollerud, E. J., et al. 2013, *A&A*, **558**, A33
- Bahcall, J. N., & Peebles, P. J. E. 1969, *ApJL*, **156**, L7
- Barkana, R., & Loeb, A. 2001, *PhR*, **349**, 125
- Barlow, T. A. 2005, MAKEE Data Reduction Package. https://www.astro.caltech.edu/~tb/ipac_staff/tab/makee/index.html
- Becker, G. D., & Bolton, J. S. 2013, *MNRAS*, **436**, 1023
- Becker, G. D., Bolton, J. S., Haehnelt, M. G., & Sargent, W. L. W. 2011, *MNRAS*, **410**, 1096
- Becker, G. D., Bolton, J. S., & Lidz, A. 2015, *PASA*, **32**, e045
- Becker, G. D., Rauch, M., & Sargent, W. L. W. 2009, *ApJ*, **698**, 1010
- Becker, G. D., Pettini, M., Rafelski, M., et al. 2019, *ApJ*, **883**, 163
- Behroozi, P. S., Wechsler, R. H., & Conroy, C. 2013, *ApJ*, **770**, 57
- Bergeron, J., & Herbert-Fort, S. 2005, in IAU Colloq. 199: Probing Galaxies through Quasar Absorption Lines, ed. P. Williams, C.-G. Shu, & B. Menard, 265–280
- Boksenberg, A., & Sargent, W. L. W. 2015, *ApJS*, **218**, 7
- Bolton, J. S., & Haehnelt, M. G. 2007, *MNRAS*, **382**, 325
- Bordoloi, R., Tumlinson, J., Werk, J. K., et al. 2014, *ApJ*, **796**, 136
- Brook, C. B., Stinson, G., Gibson, B. K., et al. 2014, *MNRAS*, **443**, 3809
- Burchett, J. N., Tripp, T. M., Prochaska, J. X., et al. 2015, *ApJ*, **815**, 91
- Cen, R., & Chisari, N. E. 2011, *ApJ*, **731**, 11
- Chen, H.-W. 2012, *MNRAS*, **427**, 1238
- Chen, H.-W., Lanzetta, K. M., & Webb, J. K. 2001, *ApJ*, **556**, 158-163
- Chen, Z.-F., Gu, Q.-S., & Chen, Y.-M. 2015, *ApJS*, **221**, 32
- Christensen, C. R., Davé, R., Governato, F., et al. 2016, *ApJ*, **824**, 57
- Churchill, C. W. 1997, PhD thesis, University of California, Santa Cruz
- Churchill, C. W., Rigby, J. R., Charlton, J. C., & Vogt, S. S. 1999, *ApJS*, **120**, 51
- Churchill, C. W., Vander Vliet, J. R., Trujillo-Gomez, S., Kacprzak, G. G., & Klypin, A. 2015, *ApJ*, **802**, 10
- Churchill, C. W., & Vogt, S. S. 2001, *AJ*, **122**, 679
- Codoreanu, A., Ryan-Weber, E. V., García, L. Á., et al. 2018, *MNRAS*, **481**, 4940
- Cooksey, K. L., Kao, M. M., Simcoe, R. A., O’Meara, J. M., & Prochaska, J. X. 2013, *ApJ*, **763**, 37
- Cooksey, K. L., Thom, C., Prochaska, J. X., & Chen, H.-W. 2010, *ApJ*, **708**, 868-908
- Cooper, T. J., Simcoe, R. A., Cooksey, K. L., et al. 2019, *ApJ*, **882**, 77
- Danforth, C. W., & Shull, J. M. 2008, *ApJ*, **679**, 194

- De Cia, A., Ledoux, C., Petitjean, P., & Savaglio, S. 2018, *A&A*, **611**, [A76](#)
- Dekel, A., & Mandelker, N. 2014, *MNRAS*, **444**, [2071](#)
- Dekker, H., et al. 2000, in Proc. SPIE, ed. M. Iye & A. F. Moorwood, Vol. 4008, 534–545
- D’Odorico, V., Calura, F., Cristiani, S., & Viel, M. 2010, *MNRAS*, **401**, [2715](#)
- . 2016, *MNRAS*, **459**, [232](#)
- D’Odorico, V., Cupani, G., Cristiani, S., et al. 2013, *MNRAS*, **435**, [1198](#)
- Doughty, C., & Finlator, K. 2019, *MNRAS*, **489**, [2755](#)
- Doughty, C., Finlator, K., Oppenheimer, B. D., Davé, R., & Zackrisson, E. 2018, *MNRAS*, **475**, [4717](#)
- Faucher-Giguère, C.-A., Lidz, A., Hernquist, L., & Zaldarriaga, M. 2008, *ApJ*, **688**, [85](#)
- Faucher-Giguère, C.-A., Lidz, A., Zaldarriaga, M., & Hernquist, L. 2009, *ApJ*, **703**, [1416](#)
- Feldmann, R., Hopkins, P. F., Quataert, E., Faucher-Giguère, C.-A., & Kereš, D. 2016, *MNRAS*, **458**, [L14](#)
- Finlator, K. 2017, in Gas Accretion onto Galaxies, ed. A. Fox & R. Davé, Vol. 430
- Finlator, K., Doughty, C., Cai, Z., & Díaz, G. 2020, *MNRAS*, **493**, [3223](#)
- Finlator, K., Keating, L., Oppenheimer, B. D., Davé, R., & Zackrisson, E. 2018, *MNRAS*, **480**, [2628](#)
- Finlator, K., Oppenheimer, B. D., Davé, R., et al. 2016, *MNRAS*, **459**, 2299–2310
- Finlator, K., Thompson, R., Huang, S., et al. 2015, *MNRAS*, **447**, [2526](#)
- Ford, A. B., Davé, R., Oppenheimer, B. D., et al. 2014, *MNRAS*, **444**, [1260](#)
- Fox, A. J., Ledoux, C., Petitjean, P., & Srianand, R. 2007, *A&A*, **473**, [791](#)
- Furlanetto, S. R. 2009, *ApJ*, **703**, [702](#)
- Gnedin, N. Y. 2000, *ApJ*, **535**, [530](#)
- Gnedin, N. Y., & Ostriker, J. P. 1997, *ApJ*, **486**, [581](#)
- Haardt, F., & Madau, P. 2012, *ApJ*, **746**, [125](#)
- Hassan, S., Finlator, K., Davé, R., Churchill, C. W., & Prochaska, J. X. 2020, *MNRAS*, **492**, [2835](#)
- Holmberg, E. 1975, in Galaxies and the Universe, ed. A. Sandage, M. Sandage, & J. Kristian, 123
- Hunter, J. D. 2007, *Computing in Science & Engineering*, **9**, 90–95
- Kacprzak, G. G., & Churchill, C. W. 2011, *ApJL*, **743**, [L34](#)
- Kacprzak, G. G., Churchill, C. W., & Nielsen, N. M. 2012, *ApJL*, **760**, [L7](#)
- Kacprzak, G. G., Churchill, C. W., Steidel, C. C., & Murphy, M. T. 2008, *AJ*, **135**, [922](#)
- Keating, L. C., Puchwein, E., Haehnelt, M. G., Bird, S., & Bolton, J. S. 2016, *MNRAS*, **461**, [606](#)
- King, J. A., Webb, J. K., Murphy, M. T., et al. 2012, *MNRAS*, **422**, [3370](#)
- Komatsu, E., Dunkley, J., Nolta, M. R., et al. 2009, *ApJS*, **180**, [330](#)
- Kulkarni, G., Worseck, G., & Hennawi, J. F. 2019, *MNRAS*, **488**, [1035](#)
- Lanzetta, K. M., Turnshek, D. A., & Wolfe, A. M. 1987, *ApJ*, **322**, [739](#)
- Lehner, N., Burchett, J. N., Howk, J. C., et al. 2019, *BAAS*, **51**, [473](#)
- Lehner, N., O’Meara, J. M., Howk, J. C., Prochaska, J. X., & Fumagalli, M. 2016, *ApJ*, **833**, [283](#)
- Liang, C. J., & Chen, H.-W. 2014, *MNRAS*, **445**, [2061](#)
- Lilly, S. J., Carollo, C. M., Pipino, A., Renzini, A., & Peng, Y. 2013, *ApJ*, **772**, [119](#)
- Madau, P., & Dickinson, M. 2014, *ARA&A*, **52**, [415](#)
- Matejek, M. S., & Simcoe, R. A. 2012, *ApJ*, **761**, [112](#)
- Mathes, N. L. 2017, PhD thesis, New Mexico State University
- McQuinn, M. 2016, *ARA&A*, **54**, [313](#)
- McQuinn, M., Lidz, A., Zaldarriaga, M., et al. 2009, *ApJ*, **694**, 842–866
- Ménard, B., Wild, V., Nestor, D., et al. 2011, *MNRAS*, **417**, [801](#)
- Misawa, T., Tytler, D., Iye, M., et al. 2002, *AJ*, **123**, [1847](#)
- Morrison, S., Pieri, M. M., Syphers, D., & Kim, T.-S. 2019, *MNRAS*, **489**, [868](#)
- Muratov, A. L., Kereš, D., Faucher-Giguère, C.-A., et al. 2015, *MNRAS*, **454**, [2691](#)
- . 2017, *MNRAS*, **468**, [4170](#)
- Murphy, E. J., Chary, R. R., Dickinson, M., et al. 2011, *ApJ*, **732**, [126](#)
- Murphy, M. T. 2016, UVES_popler: POst PipeLine Echelle Reduction software. <https://doi.org/10.5281/zenodo.56158>
- Murphy, M. T., Kacprzak, G. G., Savorgnan, G. A. D., & Carswell, R. F. 2019, *MNRAS*, **482**, [3458](#)
- Murphy, M. T., Malec, A. L., & Prochaska, J. X. 2016, *MNRAS*, **461**, [2461](#)
- Navarro, J. F., Ludlow, A., Springel, V., et al. 2010, *MNRAS*, **402**, [21](#)
- Nielsen, N. M., Churchill, C. W., Kacprzak, G. G., & Murphy, M. T. 2013, *ApJ*, **776**, [114](#)
- Nielsen, N. M., Churchill, C. W., Kacprzak, G. G., Murphy, M. T., & Evans, J. L. 2015, *ApJ*, **812**, [83](#)
- Nielsen, N. M., Kacprzak, G. G., Pointon, S. K., et al. 2020, arXiv e-prints, [arXiv:2002.08516](https://arxiv.org/abs/2002.08516)

- Oliphant, T. E. 2006, *A guide to NumPy*, Vol. 1 (Trelgol Publishing USA)
- O'Meara, J. M., Lehner, N., Howk, J. C., et al. 2015, *AJ*, **150**, 111
- Oppenheimer, B. D., & Davé, R. 2008, *MNRAS*, **387**, 577
- Oppenheimer, B. D., Davé, R., Kereš, D., et al. 2010, *MNRAS*, **406**, 2325
- Oppenheimer, B. D., Davé, R., & Finlator, K. 2009, *MNRAS*, 396, 729-758
- Parsa, S., Dunlop, J. S., McLure, R. J., & Mortlock, A. 2016, *MNRAS*, **456**, 3194
- Perez, F., & Granger, B. E. 2007, *Computing in Science Engineering*, **9**, 21-29
- Péroux, C., Petitjean, P., Aracil, B., Irwin, M., & McMahon, R. G. 2004, *A&A*, **417**, 443
- Petitjean, P., & Bergeron, J. 1994, *A&A*, **283**, 759
- Pettini, M., Madau, P., Bolte, M., et al. 2003, *ApJ*, **594**, 695
- Puchwein, E., Haardt, F., Haehnelt, M. G., & Madau, P. 2019, *MNRAS*, **485**, 47
- Rafelski, M., Wolfe, A. M., Prochaska, J. X., Neeleman, M., & Mendez, A. J. 2012, *ApJ*, **755**, 89
- Rahmati, A., Schaye, J., Crain, R. A., et al. 2016, *MNRAS*, **459**, 310
- Rauch, M., Sargent, W. L. W., Womble, D. S., & Barlow, T. A. 1996, *ApJL*, **467**, L5
- Robertson, B. E., Furlanetto, S. R., Schneider, E., et al. 2013, *ApJ*, **768**, 71
- Rupke, D. 2018, *Galaxies*, **6**, 138
- Sargent, W. L. W., Boksenberg, A., & Steidel, C. C. 1988, *ApJS*, **68**, 539
- Scannapieco, E., Pichon, C., Aracil, B., et al. 2006, *MNRAS*, **365**, 615
- Schaye, J., Aguirre, A., Kim, T.-S., et al. 2003, *ApJ*, **596**, 768
- Schaye, J., Carswell, R. F., & Kim, T.-S. 2007, *MNRAS*, **379**, 1169
- Schechter, P. 1976, *ApJ*, **203**, 297
- Schneider, D. P., Hartig, G. F., Jannuzi, B. T., et al. 1993, *ApJS*, **87**, 45
- Shankar, F., Weinberg, D. H., & Miralda-Escudé, J. 2009, *ApJ*, **690**, 20
- Shen, X., Hopkins, P. F., Faucher-Giguère, C.-A., et al. 2020, *MNRAS*, **495**, 3252
- Simcoe, R. A. 2011, *ApJ*, **738**, 159
- Simcoe, R. A., Cooksey, K. L., Matejek, M., et al. 2011, *ApJ*, **743**, 21
- Somerville, R. S., & Davé, R. 2015, *ARA&A*, **53**, 51
- Songaila, A. 2001, *ApJL*, **561**, L153
- . 2005, *AJ*, **130**, 1996
- . 2006, *AJ*, **131**, 24
- Steidel, C. C. 1990, *ApJS*, **72**, 1
- Steidel, C. C. 1993, in *Galaxy Evolution. The Milky Way Perspective*, ed. S. R. Majewski, Vol. 49, 227
- Steidel, C. C., Erb, D. K., Shapley, A. E., et al. 2010, *ApJ*, **717**, 289
- Tody, D. 1986, in *Society of Photo-Optical Instrumentation Engineers (SPIE) Conference Series*, Vol. 627, *Proc. SPIE*, ed. D. L. Crawford, 733
- Tumlinson, J., Peebles, M. S., & Werk, J. K. 2017, *ARA&A*, **55**, 389
- van de Voort, F., Schaye, J., Booth, C. M., & Dalla Vecchia, C. 2011, *MNRAS*, **415**, 2782
- Véron-Cetty, M. P., & Véron, P. 2001, *A&A*, **374**, 92
- Virtanen, P., Gommers, R., Oliphant, T. E., et al. 2020, *Nature Methods*, **17**, 261
- Vogt, S. S., et al. 1994, in *Proc. SPIE*, ed. D. L. Crawford & E. R. Craine, Vol. 2198, 362
- Worseck, G., Prochaska, J. X., Hennawi, J. F., & McQuinn, M. 2016, *ApJ*, **825**, 144
- York, D. G., et al. 2000, *AJ*, **120**, 1579
- Zackrisson, E., Inoue, A. K., & Jensen, H. 2013, *ApJ*, **777**, 39
- Zhu, G., & Ménard, B. 2013, *ApJ*, **770**, 130